

Perfluoroarene-Based 2D/3D Perovskite Solar Cells

Weifan Luo^{1#}, Jong-Min Kim^{2#}, Paul Zimmermann³, Tim Hügli¹, Sun-Ju Kim², Mengqiong Zhu¹, Ghewa AlSabeh^{1,4}, Alexander Hinderhofer³, Frank Schreiber³, Jovana V. Milić^{1}, Ji-Youn Seo^{2*}*

¹Adolphe Merkle Institute/ University of Fribourg, 1700 Fribourg, Switzerland; ²Department of Nanoenergy Engineering, Pusan National University, 46241 Busan, South Korea; ³Institute of Applied Physics, University of Tübingen, 72076 Tübingen, Germany; ⁴Laboratory of Photonics and Interfaces, École Polytechnique Fédérale de Lausanne, 1015 Lausanne, Switzerland. #Authors contributed equally.

*Corresponding author: j-y.seo@pusan.ac.kr; jovana.milic@unifr.ch. DOI:10.1021/acsaem.4c01710

Keywords: mixed-dimensional perovskites; 2D/3D perovskites; perfluoroarenes; interfacial engineering; photovoltaics.

Abstract. Hybrid organic-inorganic layered (2D) halide perovskites have demonstrated advantages in improving the performance and stability of perovskite solar cells, and there is an ongoing interest in tailoring the organic cations for their application in photovoltaics. We apply tailored molecular systems based on perfluorinated benzylammonium (F-BNA) and 1,4-phenylenedimethylammonium (F-PDMA) cations, forming Ruddlesden–Popper and Dion–Jacobson perovskite phases, respectively, at the interface with 3D perovskite layers in conventional n-i-p perovskite solar cells. The characteristics of 2D/3D perovskite phases are investigated through a combination of techniques, including X-ray diffraction, UV-vis absorption, and photoluminescence spectroscopy. We demonstrate the beneficial effects of perfluoroarene perovskite phases in improving stability and performance toward advancing photovoltaics.

Introduction

In recent years, there has been a growing interest in exploring 3D/2D perovskite structures, aiming to merge the favorable attributes of 2D and 3D perovskite materials.^{1,2} This hybrid approach seeks to capitalize on the stability inherent in 2D perovskites while harnessing the high efficiency associated with their 3D counterparts.¹ Metal halide perovskites are described by the general formula AMX_3 (Figure 1), where A denotes the central cation (e.g., methylammonium MA^+ , formamidinium FA^+ , or Cs^+), M represents a divalent metal ion (predominantly Pb^{2+} or Sn^{2+}), and X signifies a halide anion (I^- , Br^- , or Cl^-).³ Their layered (2D) perovskite analogues have gained considerable interest due to their superior stability compared to 3D perovskite materials.⁴ They are formed by introducing spacer cations between the layers of hybrid perovskites (Figure 1),⁴ leading to the formation of common Ruddlesden–Popper (RP) and Dion–Jacobson (DJ) phases.⁵ RP systems typically have the general formula $S'_2A_{n-1}M_nX_{3n+1}$, where S' denotes monofunctional spacers, resulting in the formation of a bilayer structure with a half-unit-cell displacement between adjacent layers (Figure 1). Conversely, DJ systems are characterized by the formula $SA_{n-1}M_nX_{3n+1}$, incorporating bifunctional spacer (S) moieties between aligned perovskite layers.⁶⁻⁹ Spacer cations can tune the properties of 2D perovskites, their morphology, and structure, forming a natural quantum well electronic structure and altering the band gap while serving as protective layers that increase hydrophobicity and prevent ion migration.^{4,10} There is significant interest in incorporating these materials into perovskites due to their structural diversity and stabilizing potential.¹¹ In particular, the use of mixed-dimensional 2D/3D perovskite heterostructures, with the capacity to simultaneously improve photovoltaic performances and stabilities through a synergy of 2D and 3D perovskite layers, has been especially relevant to advancing perovskite photovoltaics.^{1,2} They are accessed by depositing 2D perovskites or organic spacer cations onto 3D perovskite layers.^{1,2}

To this end, perfluorinated organic moieties are particularly noteworthy since introducing fluorine can enhance the hydrophobicity and suppress ion migration.¹² Accordingly, perfluoroarenes are of interest to tailoring structural and optoelectronic properties of 2D perovskites toward their applications.¹³⁻¹⁵ The perfluoroarene systems are relevant to controlling hybrid perovskite assemblies through π -based interactions, hydrogen bonding, van der Waals forces, as well as halogen bonding.^{4,11,13} These interactions can modify the optoelectronic and structural properties of the hybrid materials. For example, hydrogen bonding can regulate perovskite assemblies and the activation energy for ion migration.¹³ Additionally, π - π interactions between arene and perfluoroarene species can create an alternating-cation 2D perovskite system through self-assembly.¹⁶ This results in a more compact parallel (π - π) stacking in arene-perfluoroarene systems, enhancing charge transport.^{16,17,18} In this regard, the emerging 2D/3D perovskite heterostructures^{1,2,19,20,21} provide a relevant platform for perfluoroarenes. However, these (supra)molecular systems remain underexploited for their potential to tailor the properties of the interface with charge-selective extraction layers in mixed-dimensional perovskite photovoltaics.

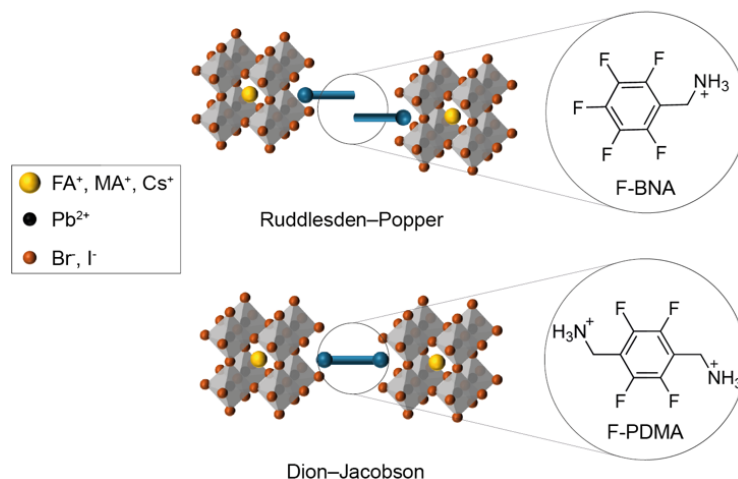


Figure 1. Layered hybrid perovskite structure. Schematic of the layered (2D) perovskite structure with the Ruddlesden-Popper (RP) and Dion-Jacobson (DJ) perovskite phase (represented by $n = 2$ compositions) and structures of perfluoro arenes F-BNA and F-PDMA employed in this study.

Here, we applied perfluorinated benzylammonium (F-BNA) and 1,4-phenylenedimethylammonium (F-PDMA) iodides as uniquely tailored model systems that form RP and DJ 2D perovskite overlayers, respectively, onto 3D perovskites in corresponding solar cells. The formation of 2D/3D heterostructures was investigated by a combination of techniques, including X-ray diffraction, X-ray photoelectron, UV-vis absorption, and photoluminescence spectroscopy. We integrated the 2D/3D perfluoroarene-based perovskite layers into n-i-p perovskite solar cells, achieving a power conversion efficiency (PCE) up to 20% for champion devices, compared to 18% for a control device without the 2D/3D structure. Moreover, the devices displayed operational stability with 85% performance retention after 750 hours, showcasing the relevance of perfluoroarene-based perovskites in photovoltaics.

Results and Discussion

The perfluoroarene spacers were synthesized by reducing tetrafluoroterephthalonitrile or pentafluorobenzonitrile precursors, followed by protonation of the resulting amines in accordance with the previous reports,^{17,18} as detailed in the Experimental Section of the Supporting Information (SI; Figures S1–S6). The spacer precursors, F-BNAI or F-PDMAI₂, were thereafter used to prepare materials by reacting them with stoichiometric amounts of PbI₂ to obtain 2D perovskites of $n = 1$ nominal composition. This was achieved through solution-processing (spin-coating) of films onto glass substrates, followed by annealing at 130 °C. The effectiveness of perfluoroarene-based 2D perovskites was thereafter analyzed in 2D/3D perovskite heterostructures by applying organic spacers from the solution of F-BNAI or F-PDMAI₂ (1 mg/mL concentration in isopropanol) onto conventional 3D (Cs_{0.05}FA_{0.83}MA_{0.17})Pb(I_{0.83}Br_{0.17})₃ compositions, forming 2D overlayers upon annealing in n-i-p perovskite solar cells, which were further investigated.

The structural properties of hybrid materials were analyzed by using X-ray diffraction (XRD). The low-angle reflections (2θ below 10 degrees) accompanied by periodic reflections indicate the formation of a layered (2D) perovskite structure (Figure 2a).²² For (F-BNA)₂PbI₄, a peak below 14° was identified, corresponding to the (004) reflection. A comparable result was obtained for the (F-PDMA)PbI₄ system. Moreover, grazing-incidence X-ray scattering (GIWAXS) measurements showed consistent results with an additional peak for (F-BNA)₂PbI₄ at 5° (0.35 Å⁻¹). Additionally, GIWAXS indicated the long unit cell axis is preferentially oriented parallel to the substrate for (F-BNA)₂PbI₄ (Figure S7), whereas for (F-PDMA)PbI₄ it was mainly oriented parallel to the surface normal, with a substantial amount of randomly oriented $n = 1$ 2D phases (Figure S8). For the F-BNA phase, we determined a unit cell consistent with GIWAXS data (Figure S9). At room temperature we found a tetragonal unit cell for (F-BNA)₂PbI₄ ($n = 1$) with the unit cell parameters $a = b = 8.55(8)$ Å, $c = 35.6(4)$ and a volume of $V = 2602(78)$ Å³ (Table S1). The optoelectronic properties of 2D phases were further analyzed by UV-vis absorption and photoluminescence (PL) spectroscopy (Figure 2b). The excitonic features in the absorption spectra at around 460 nm corroborate the formation of 2D structures.^{5,18,23} In addition, the PL spectra of F-PDMA-based films (Figure S10) exhibit multiple signals indicative of disorder, consistent with prior reports,¹⁶ which require further investigation.

Having evidenced the 2D perovskite formation, the structural properties of the 2D/3D perovskite materials were further analyzed. GIWAXS measurements were conducted to assess the effect of the spacers on the 3D perovskites (Figure S11), which showed no change in the orientation upon their use. All samples showed a preferred orientation of approximately 35° and 65° toward the substrate (Figure S12). Moreover, the control 3D sample was composed mainly of cubic perovskite and some PbI₂ traces, whereas the F-PDMA treated sample showed a peak at 0.5Å. The same peak

was found for the pure F-PDMA PbI_4 phase, indicating the formation of a 2D ($n = 1$) layer on top of the 3D perovskite accompanied by the reduction of PbI_2 and hexagonal phase in the underlying 3D perovskite layer (Figure S13). Furthermore, X-ray photoelectron spectroscopy (XPS) measurements were performed on 3D and 2D/3D perovskite films to evaluate the formation of the overlayers (Figure 2c–d) by analyzing changes in the chemical environment. The untreated (control) 3D perovskite films exhibited no detectable fluorine (F) signal, whereas a distinct F 1s core level signal emerged at 685 eV for 2D/3D perovskite films. In addition, the N 1s spectra of the 3D perovskite films featured characteristic C—N bonds (397.5 eV) associated with the A cation (Figure 2d, Table S2).²⁴ F-PDMA-treated samples exhibited a more pronounced (0.5 eV) shift toward lower binding energy compared to the control film. This indicates that the F-PDMA-based overlayer interacts more with the surface (e.g., Pb^{2+} or I^-), altering the electronic structure around nitrogen, which is more pronounced than the F-BNA systems. These interactions result in an increased electron density around the nitrogen atom, which was more pronounced compared to the C 1s XPS spectra (Figure S14), suggesting interactions predominantly taking place through the ammonium groups.²⁴ The effects of the interaction on the interfacial energetics was further analyzed using ultraviolet photoemission spectroscopy (UPS), with the bandgap estimated using photoluminescence (PL) spectra and the Tauc plots with the corresponding UV-vis absorption spectra. The work function (WF) showed differences of 0.02 eV and 0.26 eV between the reference and F-BNA or F-PDMA treated films, respectively (Figure 2e). Furthermore, the valence band (VB) maxima were 0.04 eV and 0.13 eV lower than the reference for treated films, respectively. UPS analysis confirmed that the energy level of the perovskite film changes when F-BNA or F-PDMA is applied, with the valence band (VB) tends to shift. While the energy alignment featured a minor mismatch at the hole transport layer (Figure 2f), the thickness of the overlayer did not

compromise charge transport.^{25,26} This was further analyzed by steady-state and time-resolved photoluminescence (PL) spectroscopy. The PL spectra of 2D/3D perovskites revealed a reduced intensity upon applying the 2D overlay, which can be related to an increase in non-radiative recombination due to changes in the interfacial defect concentration (Figure S15). This observation is consistent with the time-resolved photoluminescence spectroscopy (TRPL) data of the perovskite films, showing longer charge-carrier lifetimes for reference 3D perovskite materials (Figure S16, Table S3). However, in the presence of the hole-transport layer, faster decay was observed for the treated samples than in the control, suggesting that the perfluoroarene layers do not act as a barrier for charge extraction (Figure S17). By applying an exponential fit to the TRPL decays, the extraction time was estimated (Table S4), suggesting a facilitated charge extraction in the 2D/3D perovskite heterostructures to the 2,2',7,7'-tetrakis(*N,N*-di-4-methoxyphenylamino)-9,9'-spirobifluorene (Spiro-OMeTAD).²⁷ This is likely the result of arene-perfluoroarene interactions^{16,17,18} with the hole-transporting material, which were envisaged to stabilize the interface with the hole-extraction layer and improve the contacts relevant to device performance and long-term stability. Furthermore, the analysis of the morphology of the 3D/2D structures by scanning electron microscopy (SEM), showed an increased grain size in the 2D/3D perovskite samples (Figure S18), which is further relevant to their charge extraction and the photovoltaic performance. The SEM images also reveal gaps that may result from solvent evaporation or the escape of volatile molecules from the surface within the SEM chamber. The passivation effect at grain boundaries can nonetheless minimize device performance losses, whereas further optimization of the morphology offers space for improving device performances in the future.

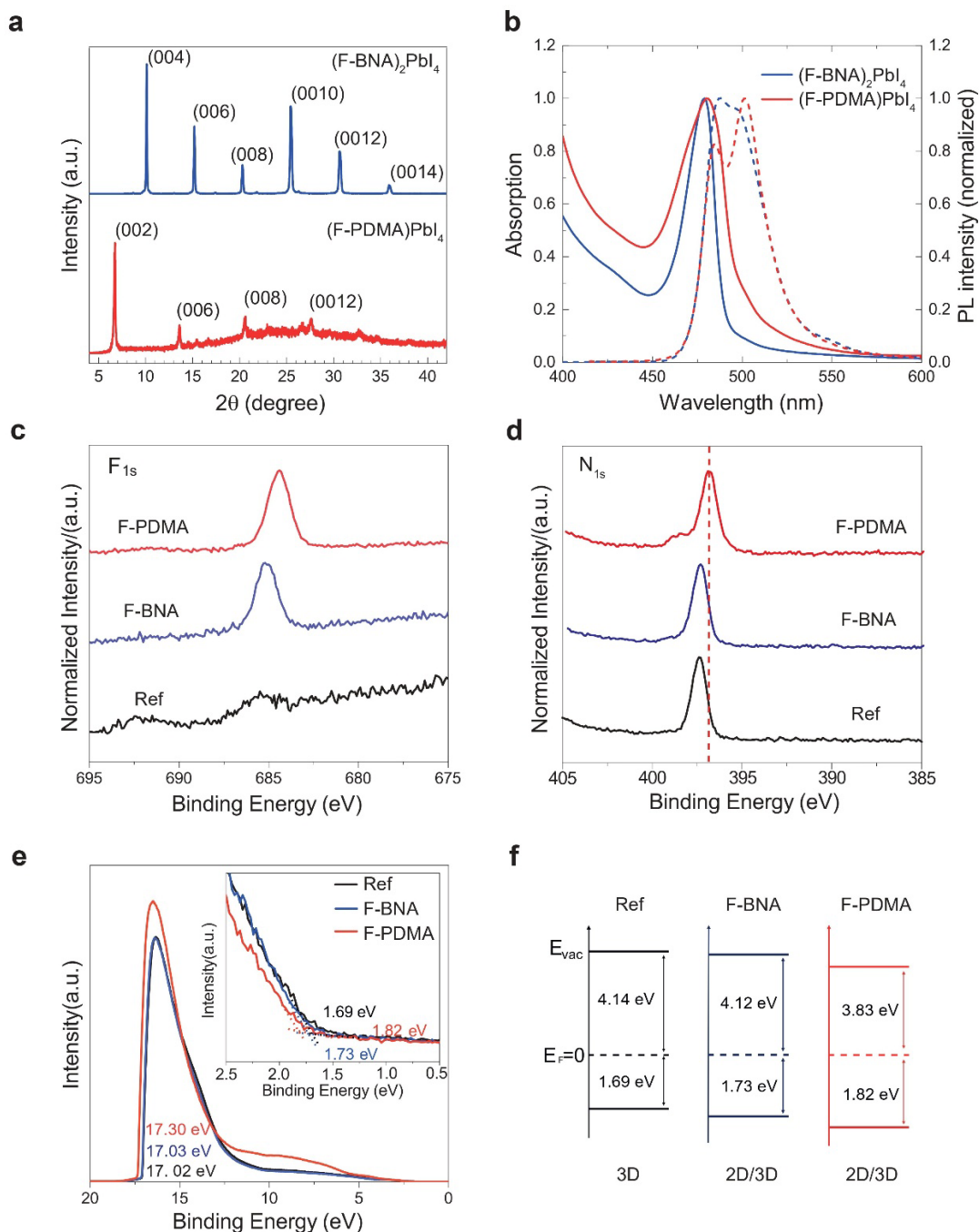


Figure 2. Structural and optoelectronic properties of 2D and 2D/3D perovskites. (a) XRD pattern, (b) UV-vis absorption and PL spectra of the perfluoroarene-based 2D perovskite films of $n = 1$ nominal composition. (c–d) XPS F 1s and N 1s core level spectra of the 3D control (Ref, black) and 3D/2D perovskite films with either F-BNA (blue) or F-PDMA (red) overlayers. (e) UPS spectra of the control (Ref) and treated (F-BNA or F-PDMA) perovskite films, with the secondary electron cut-off (SECO) for determining the work function. The binding energy of the valence band spectra is shown in the inset, and the kinetic energy is in Figure S19 of the SI. (f) Energy level diagram estimate for the perovskite samples.

The performance of 2D/3D perovskites in photovoltaics was investigated in solar cells based on n-i-p architecture of fluorine-doped tin oxide (FTO)/c-TiO₂/mp-TiO₂/perovskite/Spiro-OMeTAD/Au (Figure 3a). Their performance was evaluated by measuring the current-voltage (J - V) characteristics with a 1.5 AM light source (Figure 3b). The use of 2D/3D perovskite heterostructures with spacer overlayers resulted in increased V_{OC} and J_{SC} while maintaining an unchanged FF, thereby enhancing the overall PCE (Figure 6c). The increase in the open circuit voltage (V_{OC}) was in accordance with the passivation effect at the interface, consistent with TRPL and SEM measurements, whereas a slightly reduced bandgap (estimated to be 1.59 eV for the control and 1.55 eV for the 2D/3D perovskites) was reflected in the improvements of the photocurrent (J_{SC}), leading to the overall improved performances. The J - V curves of devices also exhibited a small hysteresis (Figure S20). The champion devices yielded PCEs of 18.4%, 20.0%, and 20.0% for the 3D, F-BNA, and F-PDMA treated samples, respectively (Table S5).

To further optimize the device performance, MACl was incorporated either by using 10 mol% into the perovskite precursor solution as an additive or by applying an overlayer (0.1; 3 mg/mL in isopropanol) onto the reference 3D perovskite (Figure S21–S24).²⁸⁻³⁰ This strategy led to an increase in V_{OC} and a slight improvement in FF, leading to an overall increase in PCE (up to 1.5%) upon treatment. Conversely, applying 2D overlayers onto these films resulted in a slight reduction in J_{SC} and FF, while V_{OC} remained comparable (Figure S25). The overall PCE remained similar, indicating that 2D overlayers did not significantly impact the MACl-treated films. The J - V curves of the champion devices showed a more significant hysteresis (Figure S26), with higher PCEs observed for champion devices of 19.9% for the 3D control, 20.2% for the MACl-based additive, 20.7% for the MACl overlayer, whereas 20.3% for the F-BNA and 20.5% for the F-PDMA treated samples. While these performances can be further optimized, the analysis suggests that the

treatment of the 3D perovskite by crystal engineering with MACl has a more pronounced effect on photovoltaic performance, whereas the 2D overlayer is expected to influence stability.

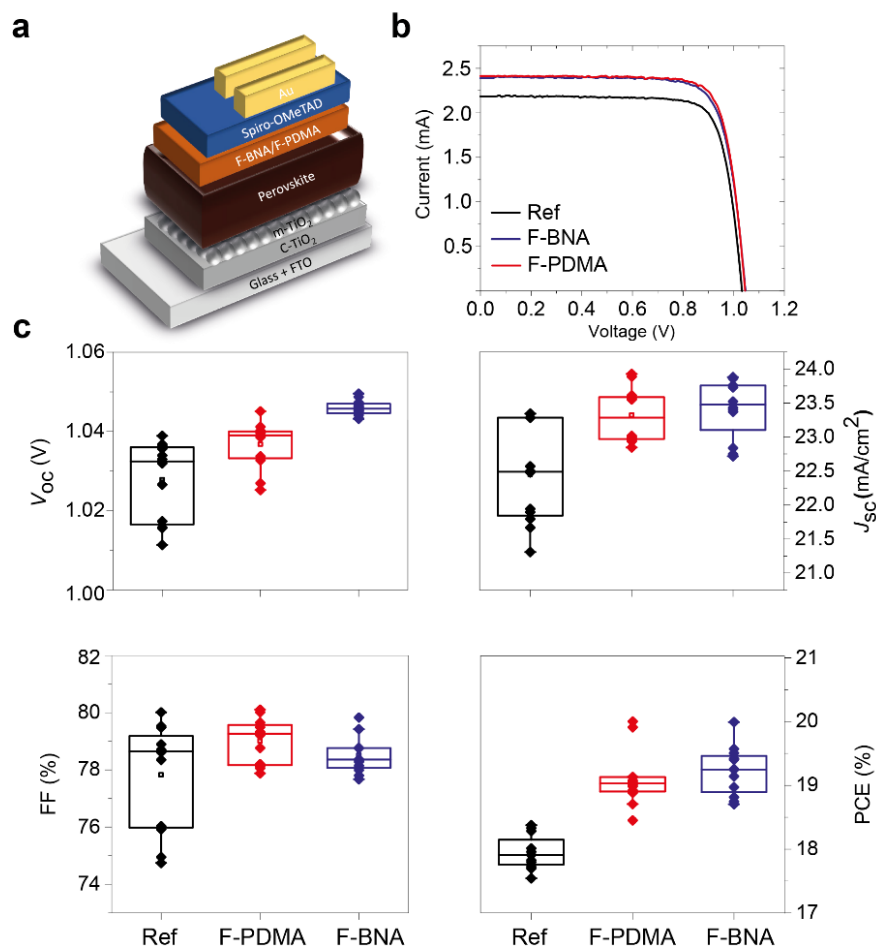


Figure 3. Photovoltaic performances in 2D/3D perovskite solar cells. (a) Schematic of the n-i-p solar cell. (b) $J-V$ curves of the champion control, F-BNA, and F-PDMA-treated devices under the AM 1.5G illumination. (c) Statistical distribution of open-circuit voltage (V_{oc}), short-circuit current density (J_{sc}), fill factor (FF), and power conversion efficiency (PCE) for control, F-BNA, and F-PDMA-treated (18) devices.

The operational stability was assessed by monitoring the evolution of the maximum power point (MPP) of n-i-p devices (2–4 devices per condition to ensure reliability) under continuous 1 sun irradiation in a nitrogen atmosphere at ambient temperature, comparing reference devices with and without MACl treatment, as well as upon the use of perfluoroarenes (Figure 4 and Figure S28). The F-BNA and F-PDMA treated samples demonstrated a significant advantage over the 3D

control devices, degrading only by around 20% after more than 500 hours (Figure 3d, S27). We observed a faster decrease in MPP at the beginning, likely due to defects at the perovskite interface, causing the initial rapid drop in MPP, which may undergo self-healing after a certain time, improving surface defects and slowing down the rate of efficiency degradation.³¹ In contrast, the reference devices with MACl showed more pronounced degradation, particularly without a 2D overlayer, with their power output decreasing by approximately 80% after 600 hours (Figure S28). These improvements in operational stability can be associated with the interactions at the interface and increased hydrophobicity upon treatment, as evidenced by contact angle measurements with a water droplet (Figure 4b and S28). The increase in the hydrophobicity is further relevant to the improvement in the contacts with the hole-transport layer, corroborating the structural and optoelectronic characteristics, which underscore the impact of perfluoroarenes in photovoltaics.

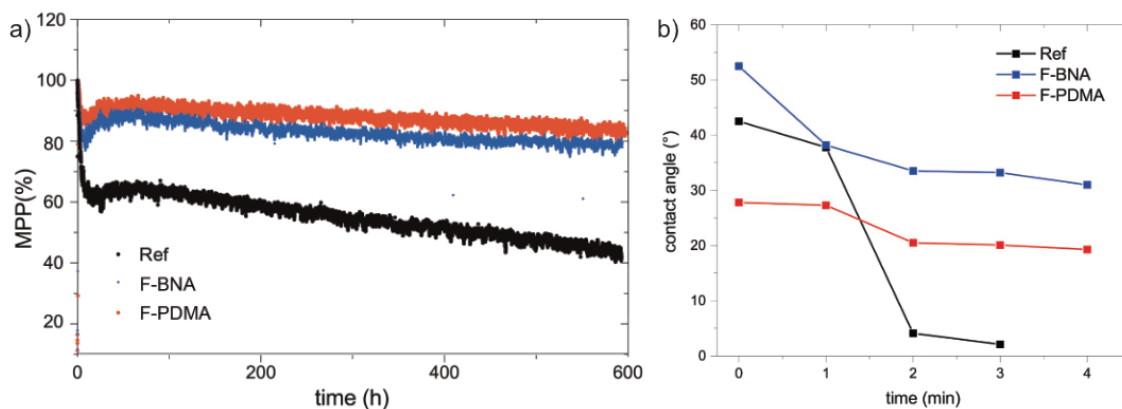


Figure 4. Operational stability in 2D/3D perovskite solar cells. (a) The evolution of the PCE during operation by MPP tracking optimized control, F-BNA, and F-PDMA-treated solar cells (with MACl additive to the 3D perovskite) in a nitrogen atmosphere under 1 sun irradiation at ambient temperature. (b) Contact angle measurement of a water droplet on the surface over time of 3D perovskite films (Ref) and 3D/2D films with F-PDMAI₂ (red) or F-BNAI (blue) overlayer.

Conclusion

In summary, we explored the use of perfluoroarene functionalized organic spacers, namely perfluoroarene benzylammonium (F-BNA) and 1,4-phenylenedimethylammonium (F-PDMA) iodide, in 2D/3D perovskite photovoltaics. We demonstrated the formation of layered (2D) perovskite materials and their 2D/3D heterostructures by a combination of structural and optoelectronic characterization. The materials were incorporated into solar cell devices, with 20% performance loss after 750 h. The performance could be further improved by adding MACl to the 3D perovskite. However, combining the 2D overlayer with MACl did not result in additional performance gains. Furthermore, the 2D overlayers significantly enhanced operational stability compared to those without the 2D layer, maintaining high performance with only ~15-20% degradation over 600 hours, compared to ~80% degradation without the 2D overlayer. This study highlights the potential of hybrid perfluoroarene-based perovskite materials in photovoltaics, providing the proof-of-concept that sets the stage for further improving device performances.

Corresponding Author

*Ji-Youn Seo. Email: j-y.seo@pusan.ac.kr; Jovana V. Milić. Email: jovana.milic@unifr.ch

Author Contributions. The project was conceptualized by J.V.M. and led by W.L., who conducted the characterization of the thin films and fabrication of the solar cell devices with T.H., who synthesized the perfluoroarene precursors with M.Z. under the supervision of J.V.M. In addition, J.K. measured XPS and UPS with the support of S.-J.K., under the supervision of J.-S.K., while G.A. performed TRPL characterization. P.Z. performed GIWAXS measurements under the supervision of A.H. and F.S. All authors have approved the manuscript.

Funding Sources. The Swiss National Science Foundation (SNSF) project no. 193174, Swiss Leading House for Asia (project SupraFlexi), and the fellowship of the Swiss Leading House for the Latin American Region.

Notes. The authors declare no competing interests.

Supporting Information. Materials and Methods, Supplementary Data. The Supporting Information is available on x. The data presented here can be accessed at DOI: xxxx (Zenodo) under the license CC-BY-4.0 (Creative Commons Attribution-ShareAlike 4.0 International).

Acknowledgment. W.L., G.A., and J.V.M. acknowledge funding from the Swiss National Science Foundation (SNSF) PRIMA project no. 193174 and the fellowship from the Swiss Leading House for the Latin American Region. J.V.M. and J-Y.S. acknowledge the Swiss Leading House for Asia (South Korea, project abbreviated as “SupraFlexi”) for supporting complementary experiments. M.Z. and J.V.M. grateful to the CSC. J.V.M. is grateful to the NCCR Bio-Inspired Materials program for support. J-Y.S. acknowledges funding from the 2024 BK21 FOUR Program of Pusan National University. The authors are grateful to Patricia Gaina and Ethan Lim for establishing the synthetic procedures. They also thank Prof. Ullrich Steiner (Adolphe Merkle Institute) and Prof. Michael Graetzel (EPFL), colleagues at the Laboratory of Photonics and Interfaces at EPFL in Switzerland, and other international collaborators for their support. A.H. acknowledges funding from the BMBF (ERUM-Pro) project 05K19VTA. We acknowledge the ESRF for the provision of synchrotron facilities, and we would like to thank Dmitry Chernyshov and Vadim Dyadkin for assistance in using beamline BM01.

REFERENCES

- (1) Grancini, G.; Roldán-Carmona, C.; Zimmermann, I.; Mosconi, E.; Lee, X.; Martineau, D.; Nabey, S.; Oswald, F.; De Angelis, F.; Graetzel, M.; Nazeeruddin, M. K. One-Year stable perovskite solar cells by 2D/3D interface engineering. *Nat. Commun.* **2017**, *8*, 15684.
- (2) Teale, S.; Degani, M.; Chen, B.; Sargent, E. H.; Grancini, G. Molecular Cation and Low-Dimensional Perovskite Surface Passivation in Perovskite Solar Cells. *Nat. Energy* **2024**, *9*, 779–792.
- (3) Jena, A. K.; Kulkarni, A.; Miyasaka, T. Halide Perovskite Photovoltaics: Background, Status, and Future Prospects. *Chem. Rev.* **2019**, *119*, 3036–3103.
- (4) Li, X.; Hoffman, J. M.; Kanatzidis, M. G. The 2D Halide Perovskite Rulebook: How the Spacer Influences Everything from the Structure to Optoelectronic Device Efficiency. *Chem. Rev.* **2021**, *121*, 2230–2291.
- (5) Blancon, J.-C.; Even, J.; Stoumpos, C. C.; Kanatzidis, M. G.; Mohite, A. D. Semiconductor physics of organic–inorganic 2D halide perovskites. *Nat. Nanotechnol.* **2020**, *15*, 969–985.
- (6) Mao, L.; Ke, W.; Pedesseau, L.; Wu, Y.; Katan, C.; Even, J.; Wasielewski, M. R.; Stoumpos, C. C.; Kanatzidis, M. G. Hybrid Dion–Jacobson 2D Lead Iodide Perovskites. *J. Am. Chem. Soc.* **2018**, *140*, 3775–3783.
- (7) Zhang, F.; Park, S. Y.; Yao, C.; Lu, H.; Dunfield, S. P.; Xiao, C.; Uličná, S.; Zhao, X.; Du Hill, L.; Chen, X.; Wang, X.; Mundt, L. E.; Stone, K. H.; Schelhas, L. T.; Teeter, G.; Parkin, S.; Ratcliff, E. L.; Loo, Y.-L.; Berry, J. J.; Beard, M. C.; Yan, Y.; Larson, B. W.; Zhu, K. Metastable Dion–Jacobson 2D structure enables efficient and stable perovskite solar cells. *Science* **2022**, *375*, 71–76.
- (8) Guo, W.; Yang, Z.; Dang, J.; Wang, M. Progress and perspective in Dion–Jacobson phase 2D layered perovskite optoelectronic applications. *Nano Energy* **2021**, *86*, 106129.

- (9) Liu, P.; Han, N.; Wang, W.; Ran, R.; Zhou, W.; Shao, Z. High-quality Ruddlesden-Popper perovskite film formation for high-performance perovskite solar cells. *Adv. Mater.* **2021**, *33*, 2002582.
- (10) Pitaro, M.; Pau, R.; Duim, H.; Mertens, M.; Van Gompel, W. T. M.; Portale, G.; Lutsen, L.; Loi, M. A. Tin-lead-metal halide perovskite solar cells with enhanced crystallinity and efficiency by addition of fluorinated long organic cation. *Appl. Phys. Rev.* **2022**, *9*, 021407.
- (11) Milić, J. V. Multifunctional layered hybrid perovskites. *J. Mater. Chem. C* **2021**, *9*, 11428–11443.
- (12) Mitzi, D. B.; Medeiros, D. R.; Malenfant, P. R. L. Intercalated Organic–Inorganic Perovskites Stabilized by Fluoroaryl–Aryl Interactions. *Inorg. Chem.* **2002**, *41*, 2134–2145.
- (13) Milić, J. V. Perfluoroarenes: A Versatile Platform for Hybrid Perovskite Photovoltaics. *J. Phys. Chem. Lett.* **2022**, *13*, 9869–9874.
- (14) Liu, Y.; Akin, S.; Pan, L.; Uchida, R.; Arora, N.; Milić, J. V.; Hinderhofer, A.; Schreiber, F.; Uhl, A. R.; Zakeeruddin, S. M.; Hagfeldt, A.; Dar, M. I.; Grätzel, M. Ultrahydrophobic 3D/2D fluoroarene bilayer-based water-resistant perovskite solar cells with efficiencies exceeding 22%. *Sci. Adv.* **2019**, *5*, eaaw2543.
- (15) Hu, J.; Oswald, I. W.; Stuard, S. J.; Nahid, M. M.; Zhou, N.; Williams, O. F.; Guo, Z.; Yan, L.; Hu, H.; Chen, Z. Synthetic control over orientational degeneracy of spacer cations enhances solar cell efficiency in two-dimensional perovskites. *Nat. Commun.* **2019**, *10*, 1276.
- (16) Almalki, M.; Dučinskas, A.; Carbone, L. C.; Pfeifer, L.; Piveteau, L.; Luo, W.; Lim, E.; Gaina, P. A.; Schouwink, P. A.; Zakeeruddin, S. M. Nanosegregation in arene-perfluoroarene π -systems for hybrid layered Dion–Jacobson perovskites. *Nanoscale* **2022**, *14*, 6771–6776.
- (17) Hope, M. A.; Nakamura, T.; Ahlawat, P.; Mishra, A.; Cordova, M.; Jahanbakhshi, F.; Mladenović, M.; Runjhun, R.; Merten, L.; Hinderhofer, A.; Carlsen, B. I.; Kubicki, D. J.; Gershoni-Poranne, R.; Schneeberger, T.; Carbone, L. C.; Liu, Y.; Zakeeruddin, S. M.; Lewinski, J.; Hagfeldt, A.;

- Schreiber, F.; Rothlisberger, U.; Grätzel, M.; Milić, J. V.; Emsley, L. Nanoscale Phase Segregation in Supramolecular π -Templating for Hybrid Perovskite Photovoltaics from NMR Crystallography. *J. Am. Chem. Soc.* **2021**, *143*, 1529–1538.
- (18) Li, Y.; Milić, J. V.; Ummadisingu, A.; Seo, J.-Y.; Im, J.-H.; Kim, H.-S.; Liu, Y.; Dar, M. I.; Zakeeruddin, S. M.; Wang, P.; Hagfeldt, A.; Grätzel, M. Bifunctional Organic Spacers for Formamidinium-Based Hybrid Dion–Jacobson Two-Dimensional Perovskite Solar Cells. *Nano Lett.* **2019**, *19*, 150–157.
- (19) Sidhik, S.; Metcalf, I.; Li, W.; Kodalle, T.; Dolan, C. J.; Khalili, M.; Hou, J.; Mandani, F.; Torma, A.; Zhang, H.; Garai, R.; Persaud, J.; Marciel, A.; Muro Puente, I. A.; Reddy, G. N. M.; Balvanz, A.; Alam, M. A.; Katan, C.; Tsai, E.; Ginger, D.; Fenning, D. P.; Kanatzidis, M. G.; Sutter-Fella, C. M.; Even, J.; Mohite, A. D. Two-Dimensional Perovskite Templates for Durable, Efficient Formamidinium Perovskite Solar Cells. *Science* **2024**, *384*, 1227–1235.
- (20) Zhao, W.; Wu, M.; Liu, Z.; Yang, S.; Li, Y.; Wang, J.; Yang, L.; Han, Y.; Liu, S. (Frank). Orientation Engineering via 2D Seeding for Stable 24.83% Efficiency Perovskite Solar Cells. *Adv. Energy Mater.* **2023**, *13*, 2204260.
- (21) Li, P.; Zhang, Y.; Liang, C.; Xing, G.; Liu, X.; Li, F.; Liu, X.; Hu, X.; Shao, G.; Song, Y. Phase Pure 2D Perovskite for High-Performance 2D–3D Heterostructured Perovskite Solar Cells. *Adv. Mater.* **2018**, *30*, 1805323.
- (22) Tan, W. L.; McNeill, C. R. X-ray diffraction of photovoltaic perovskites: Principles and applications. *Appl. Phys. Rev.* **2022**, *9*, 021310
- (23) Alanazi, A. Q.; Almalki, M. H.; Mishra, A.; Kubicki, D. J.; Wang, Z.; Merten, L.; Eickemeyer, F. T.; Zhang, H.; Ren, D.; Alyamani, A. Y.; Albrithen, H.; Albadri, A.; Alotaibi, M. H.; Hinderhofer, A.; Zakeeruddin, S. M.; Schreiber, F.; Hagfeldt, A.; Emsley, L.; Milić, J. V.;

- Graetzel, M. Benzylammonium-Mediated Formamidinium Lead Iodide Perovskite Phase Stabilization for Photovoltaics. *Adv. Funct. Mater.* **2021**, *31*, 2101163.
- (24) Chen, P.; Bai, Y.; Wang, S.; Lyu, M.; Yun, J.-H.; Wang, L. In Situ Growth of 2D Perovskite Capping Layer for Stable and Efficient Perovskite Solar Cells. *Adv. Funct. Mater.* **2018**, *28*, 1706923.
- (25) Zouhair, S.; Yoo, S. M.; Bogachuk, D.; Herterich, J. P.; Lim, J.; Kanda, H.; Son, B.; Yun, H. J.; Würfel, U.; Chahboun, A. Employing 2D-perovskite as an electron blocking layer in highly efficient (18.5%) perovskite solar cells with printable low temperature carbon electrode. *Adv. Energy Mater.* **2022**, *12*, 2200837.
- (26) Luo, L.; Zeng, H.; Wang, Z.; Li, M.; You, S.; Chen, B.; Maxwell, A.; An, Q.; Cui, L.; Luo, D. Stabilization of 3D/2D perovskite heterostructures via inhibition of ion diffusion by cross-linked polymers for solar cells with improved performance. *Nat. Energy* **2023**, *8*, 294–303.
- (27) Stolterfoht, M.; Wolff, C. M.; Márquez, J. A.; Zhang, S.; Hages, C. J.; Rothhardt, D.; Albrecht, S.; Burn, P. L.; Meredith, P.; Unold, T. Visualization and suppression of interfacial recombination for high-efficiency large-area pin perovskite solar cells. *Nat. Energy* **2018**, *3*, 847–854.
- (28) Chen, A. Z.; Foley, B. J.; Ma, J. H.; Alpert, M. R.; Niezgoda, J. S.; Choi, J. J. Crystallographic orientation propagation in metal halide perovskite thin films. *J. Mater. Chem. A* **2017**, *5*, 7796–7800.
- (29) Deng, L.; Yang, H.; Liu, Z.; Yang, X.; Huang, Z.; Yu, H.; Wang, K.; Li, J. Effective Phase Control for High-Performance Red-Light-Emitting Quasi-2D Perovskite Solar Cells via MACl Additive. *ACS Appl. Energy Mater.* **2021**, *4*, 2856–2863.
- (30) Ma, Q.; Zhang, Y.; Lu, C.; Zhang, R.; Wang, X.; Zhang, W.; Jiang, Z. MACl-Induced Controlled Crystallization in Sequentially Deposited Perovskites for High-Efficiency and Stable Perovskite Solar Cells. *Coatings* **2023**, *13*, 1885.

- (31) Boyd, C. C.; Cheacharoen, R.; Leijtens, T.; McGehee, M. D. Understanding degradation mechanisms and improving stability of perovskite photovoltaics. *Chem. Rev.* **2018**, *199*, 3418–3451.

Supporting Information

Perfluoroarene-Based 2D/3D Perovskite Solar Cells

Weifan Luo^{1#}, Jong-Min Kim^{2#}, Paul Zimmermann³, Tim Hügli¹, Sun-Ju Kim², Mengqiong Zhu¹, Ghewa AlSabeh^{1,4}, Alexander Hinderhofer³, Frank Schreiber³, Jovana V. Milić^{1}, Ji-Youn Seo^{2*}*

¹Adolphe Merkle Institute/ University of Fribourg, 1700 Fribourg, Switzerland; ²Department of Nanoenergy Engineering, Pusan National University, 46241 Busan, South Korea; ³Institute of Applied Physics, University of Tübingen, 72076 Tübingen, Germany; ⁴Laboratory of Photonics and Interfaces, École Polytechnique Fédérale de Lausanne, 1015 Lausanne, Switzerland. [#]These authors contributed equally. *Corresponding author: jovana.milic@unifr.ch, j-y.seo@pusan.ac.kr

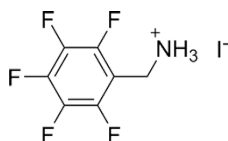
Table of Contents

Experimental Section	2
Supporting data	6
Reference	22

Experimental Section

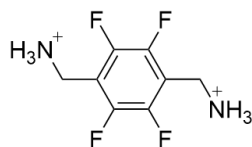
Materials

Cesium iodide (CsI) and hydrogen iodide (HI) aqueous solutions (57%) were purchased from Sigma Aldrich. Lead iodide (PbI₂) was purchased from Alfa Co. Ltd. Formamidineum iodide (FAI), methylammonium bromide (MABr) and 2,2',7,7'-tetrakis[*N,N*-di(4-methoxyphenyl)-amino]-9,9'-spirobifluorene (spiro-OMeTAD) were purchased from Lumtec. Ultra-dry *N,N*-dimethylformamide (DMF), ultra-dry dimethyl sulfoxide (DMSO), ethanol (EtOH), and ultra-dry chlorobenzene (CB) were purchased from Acros. Dry isopropanol (IPA), diethyl ether (DEE), 4-*tert*-butyl pyridine (tbp), lithium bistrifluorosulfonyl imide (Li-TFSI), acetylacetone, phenethylamine and titanium diisopropoxide bis(acetylacetonate), 75 weight % in IPA were purchased from Sigma-Aldrich. All the chemicals were used as received without further purification. Conductive glass, FTO (10 ohms/sq), was purchased from Nippon Sheet Glass, and titanium dioxide paste (30 NR-D) was purchased from Dyesol.



(*Perfluorophenyl*)methylaminium iodide (**F-BNAI**) was synthesised by following the previously reported procedure.¹ 2,3,4,5,6-pentafluorobenzonitrile (500 mg, 0.319 mL, 2.59 mmol) was added in a round bottom flask and flushed with nitrogen. BH₃ (1.0 M in THF, 6.5 mL, 6.5 mmol) was added dropwise to a suspension of 2,3,4,5,6-pentafluoro-benzonitrile in anhydrous THF (5 mL) at 0 °C. The mixture was stirred for 12 h before EtOH (10 mL) was added with vigorous stirring, and the solution was evaporated in vacuo. HI (0.85 mL, 6.47 mmol, 57%) was added at 0 °C, and a white precipitate formed immediately. After 6 h, EtOH (10 mL) was added, and the solution was concentrated in vacuo. DEE (150 mL) was then added to induce precipitation. The mixture was filtered, and the resultant solid was dried under vacuum to obtain **F-BNAI** as a white powder (460.8 mg, 54.75 %).

¹H NMR (400 MHz, (CD₃)₂SO): δ = 8.28 (bs, 3H), 4.18 (s, 2H) ppm; ¹³C NMR (101 MHz, (CD₃)₂SO): δ = 146.94–136.09, 108.5, 30.38 ppm; ¹⁹F NMR (377 MHz, (CD₃)₂SO): δ = -140.1, -152.5, -162.4 ppm



(*Perfluoro-1,4-phenylene*)dimethylammonium iodide (**F-PDMAI₂**) was synthesized following the previously reported procedure.²⁻³ 2,3,5,6-tetrafluoroterephthalonitrile (500 mg, 2.5 mmol) was added and flushed with nitrogen. BH₃ (1.0 M in THF, 11.24 mL, 11.24 mmol) was added dropwise to a suspension of 2,3,5,6-tetrafluoro-terephthalonitrile in anhydrous THF (15 mL) at 0 °C. The mixture was stirred for 36 h. After that, EtOH (20 mL) was added, and the solution was evaporated in vacuo to form a yellow solution. HI (1.48 mL, 11.24 mmol) was added at 0 °C and stirred for 6 h, resulting in a white suspension. The mixture was concentrated in vacuo to yield a white paste, over which EtOH (5 mL) was added, and the resultant suspension was added dropwise into DEE (150 mL). The mixture was allowed to crystallize overnight and it was filtered and washed with DEE (with a few drops of IPA added on the final wash). The resultant solid was dried under vacuum to obtain **F-PDMAI₂** (752 mg, 65%) as a white powder.

¹H NMR (400 MHz, (CD₃)₂SO): δ = 8.34 (bs, 6H), 4.24 (s, 4H) ppm; ¹³C NMR (101 MHz, (CD₃)₂SO): δ = 146.3–143.7, 114.5, 30.9 ppm; ¹⁹F NMR (377 MHz, (CD₃)₂SO): δ = -140.6 ppm

Perovskite thin film preparation

All samples were prepared in a glovebox under dry nitrogen atmosphere (0 ppm H₂O, 0.1–5 ppm O₂). Films were prepared on microscope glass or conductive fluorine doped tin oxide (FTO) glass, as indicated in the corresponding methods. The glass was cut from microscope slides to dimensions of 15x25 mm. The glasses were cleaned using Hellmanex (2%, deionized water), deionized water, isopropanol (IPA), and ethanol by sonicating for 10–15 min. Subsequently, the substrates were dried with nitrogen and stored until use in a dry box. The substrates were cleaned in UV-ozone plasma for 5–10 min before solution deposition. Solutions of 1 mg/mL F-BNA-I in IPA, 1 mg/mL of F-PDMAI₂ in IPA, and 0.4 M (F-BNA)₂PbI₄ or 0.4 M (F-PDMA)PbI₄ in 4:1 DMF/DMSO, were prepared using stoichiometric amounts of the precursors followed by heating to 60 °C. 40 µl of the respective solution was spread on the glass before starting the spin-coating program with a maximum rotation speed of 4000 rpm and acceleration of 2000 rpm/s with a duration of 20 s, followed by annealing at 130 °C for 10 min.

Device preparation

Etched fluorine-doped tin oxide (FTO) conductive glasses were used for device preparation. They were cleaned using Hellmanex (2%, deionized water), deionized water, isopropanol, and ethanol by sonicating for 10–15 min for each solvent. Subsequently, the glasses were dried with a nitrogen gun and stored until use in a dry box. Before further processing, the glass substrates were cleaned in UV-ozone plasma for 5–10 min.

As part of an electron-conducting layer, a compact TiO_2 (c- TiO_2) layer was deposited on the glasses using spray pyrolysis with O_2 as a carrier gas. The substrates were preheated to 450 °C, and a precursor solution consisting of 0.6 mL titaniumdiisopropoxide bis(acetylacetonate), 75 wt% in IPA, 0.4 mL acetylacetone and 9 mL dry ethanol was used. After the spray pyrolysis, the TiO_2 coated glasses were kept at 450 °C for 5 min before cooling down to room temperature. On top of the compact TiO_2 layer, a mesoporous TiO_2 (m- TiO_2) layer was deposited by spin coating for 20 s at 4000 rpm with an acceleration of 2000 rpm/s. For the m- TiO_2 layer, a solution of TiO_2 paste (30NRD, Dyesol) diluted in anhydrous ethanol at a weight ratio of 1:6 was used. After drying at 100 °C, the glasses were sintered at 450 °C for 30 min.

The perovskite precursor solution was prepared by dissolving a mixture of PbI_2 (1.61 mmol, 742.0 mg), FAI (1.31 mmol, 224.4 mg), MABr (0.15 mmol, 16.2 mg), and CsI (0.08 mmol, 19.8 mg) to yield $\text{Cs}_{0.05}\text{FA}_{0.85}\text{MA}_{0.10}\text{Pb}(\text{I}_{0.97}\text{Br}_{0.03})_3$ with 5% excess of PbI_2 in 1 mL of a mixed solution of DMF and DMSO [DMF (v): DMSO (v) = 4:1] under mild heating conditions at 70 °C to assist dissolving. For precursor solutions containing MACl, 10 mol% was added. The perovskite precursor solution was deposited on the substrates via spin-coating using an antisolvent method with CB as the antisolvent. The spin-coating program consisting of two steps was carried out first with 2000 rpm and an acceleration rate of 200 rpm/s for 10 sec followed by 6000 rpm and an acceleration rate of 2000 rpm/s for 30 sec. CB (200 μL) was dripped 15 sec before the second step ended with a 1–2 sec depositing time. The samples were annealed at 120 °C for 20 min.

For F-BNAI and F-PDMAI₂ 2D/3D overlayer, 1 mg/mL of F-BNAI or F-PDMAI₂ were dissolved in IPA and 40 μL dynamically spin-coated on the surface of the perovskite layer at 4000 rpm for 20 s with 5 min annealing at 130 °C. *For samples treated with a MACl overlayer*, 4 mg/mL of MACl in IPA were dynamically coated at 4000 rpm for 20 s with 5 min annealing at 120 °C. The preparation was carried out in a dry air-filled glove box with a relative humidity of about 2%.

For the hole-transporting layer, Spiro-OMeTAD was dissolved in CB for a concentration of 77.6 mM. 1 mL spiro-OMeTAD solution was doped with 20.6 μ L Li-TFSI (520 mg/mL in acetonitrile) and 35.5 μ L tBP. The mixed spiro-OMeTAD solution was dynamically spin-coated on the surface of the perovskite at 4000 rpm for 20 sec.

The gold electrode was thermally evaporated under vacuum onto the spiro-OMeTAD layer of the samples with a shadow mask with an aperture area of 5 mm by 5 mm. The thickness of the gold electrode was adjusted to 80 nm.

Characterization

Grazing Incidence Wide Angle X-ray Scattering (GIWAXS) was measured at the ESRF synchrotron at Beamline BM01. For the scan a PILATUS2M detector was used and a Beam energy of 11.941 keV. The incident angle was scanned from 0-2° to obtain both surface and bulk sensitive data.

X-ray diffraction measurements were conducted using a PANalytical Empyrean Series 2 instrument in Bragg-Brentano configuration. The instrument utilized Cu K α radiation with a voltage of 40 kV and a current of 40 mA. For the specific purpose of grazing incidence measurements, the X-ray incidence angle was set at 2°. Diffracted X-rays were detected during the experiments employing a PIXcel3D detector.

X-ray photoelectron spectroscopy (AXIS SUPRA) was performed with an Al K α radiation source, and all binding energies were calibrated by C 1s (248.8 eV) as a reference.

UV-vis absorption spectroscopy was conducted using a Shimadzu UV-2600 spectrophotometer.

Photoluminescence spectroscopy was performed using a Fluorolog 322 spectrometer (Horiba Jobin Yvon iHr320) equipped with a CCD detector, using a slit width of 5 nm, and the excitation by a Xenon lamp at a wavelength of 350 nm. The band slit width during the measurements was set to 5 nm.

Time-Resolved Photoluminescence (TRPL) was measured via time-correlated single photon counting (TCSPC) using a LifeSpec II (Edinburgh Instruments) fluorescence spectrometer with a picosecond pulsed diode laser (EPL-510, Edinburgh Instruments) at 510 nm wavelength.

Supporting data

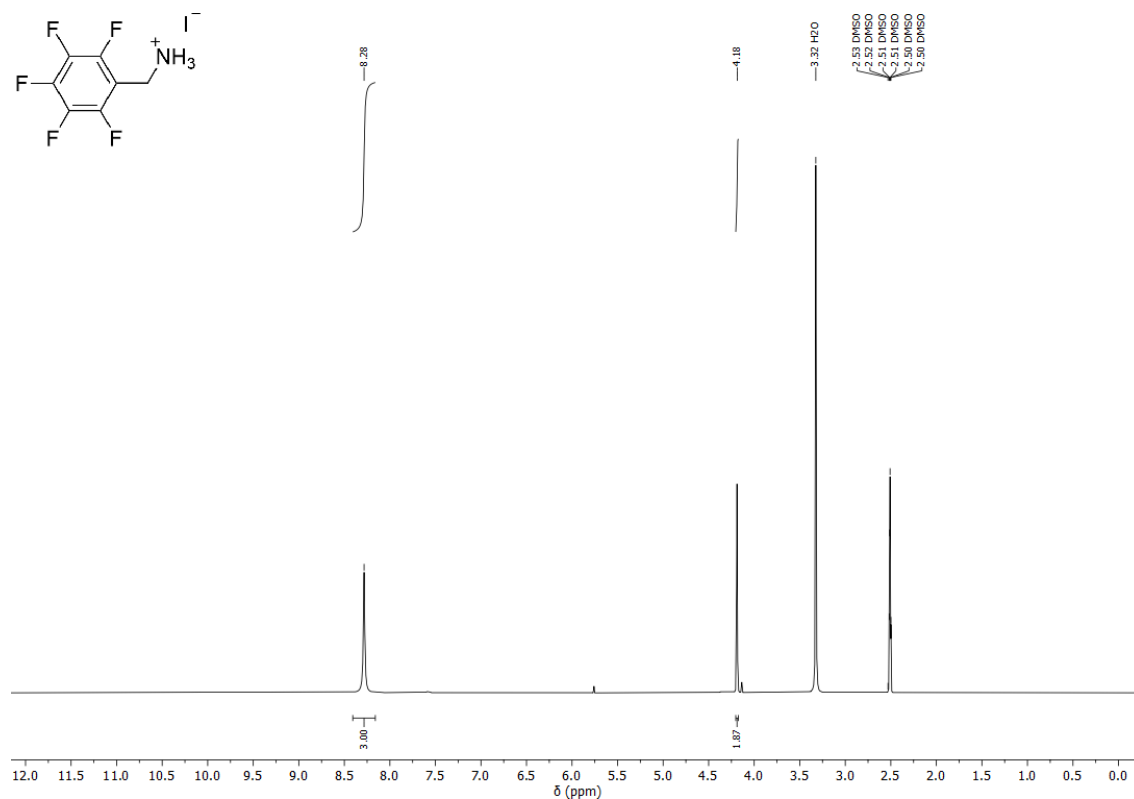


Figure S1. ^1H NMR of F-BNAI in $(\text{CD}_3)_2\text{SO}$ (400 MHz, 298 K).

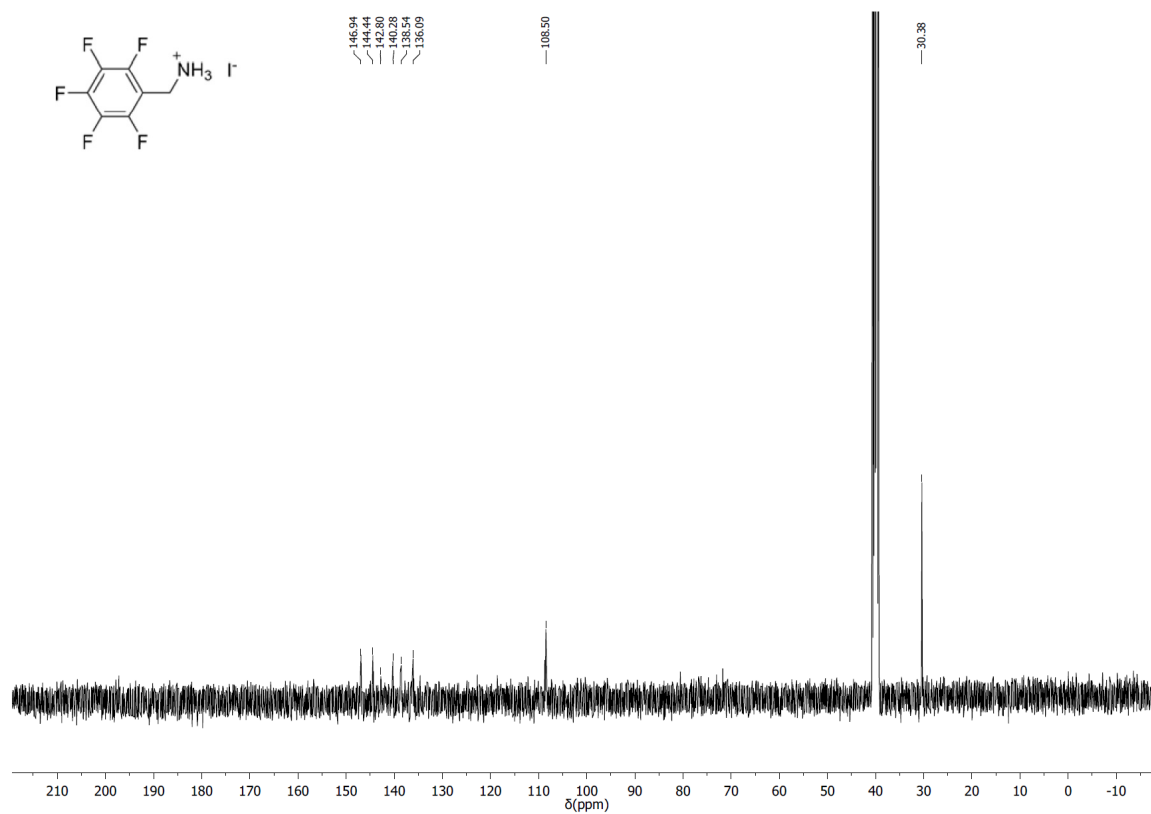


Figure S2. ^{13}C NMR of F-BNAI in $(\text{CD}_3)_2\text{SO}$ (101 MHz, 298 K).

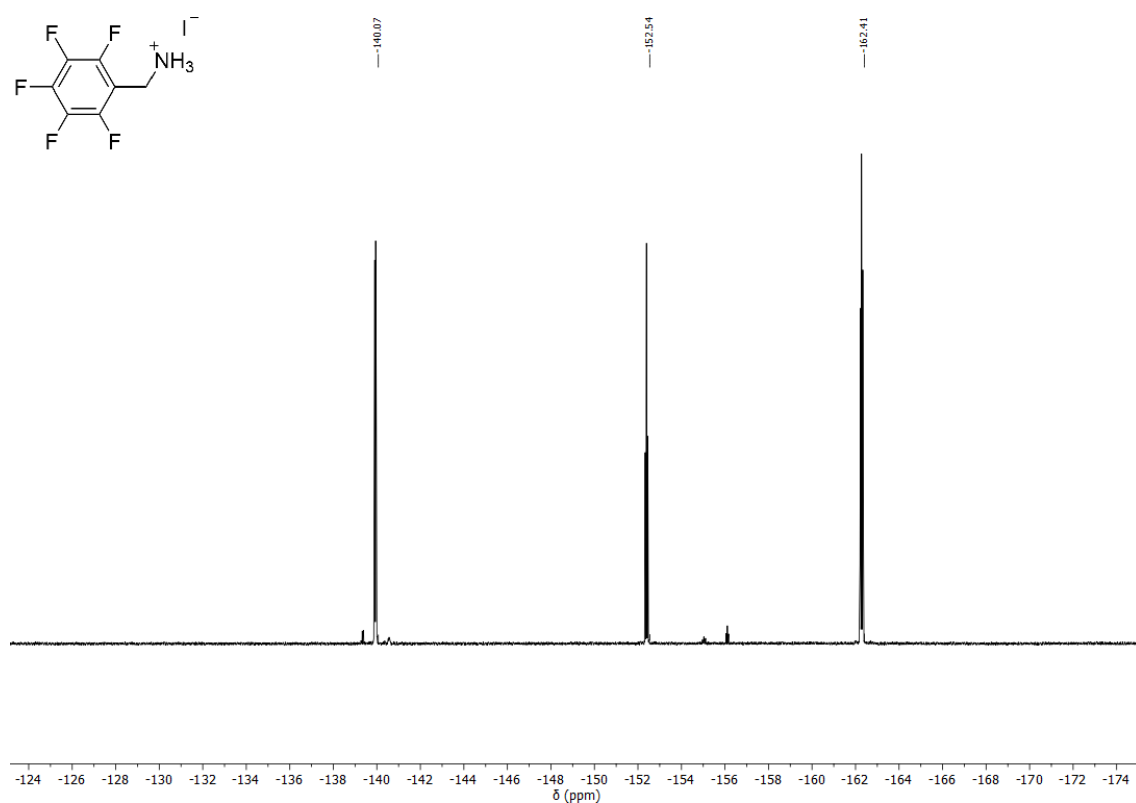


Figure S3. ^{19}F NMR of F-BNAI in $(\text{CD}_3)_2\text{SO}$ (377 MHz, 298 K).

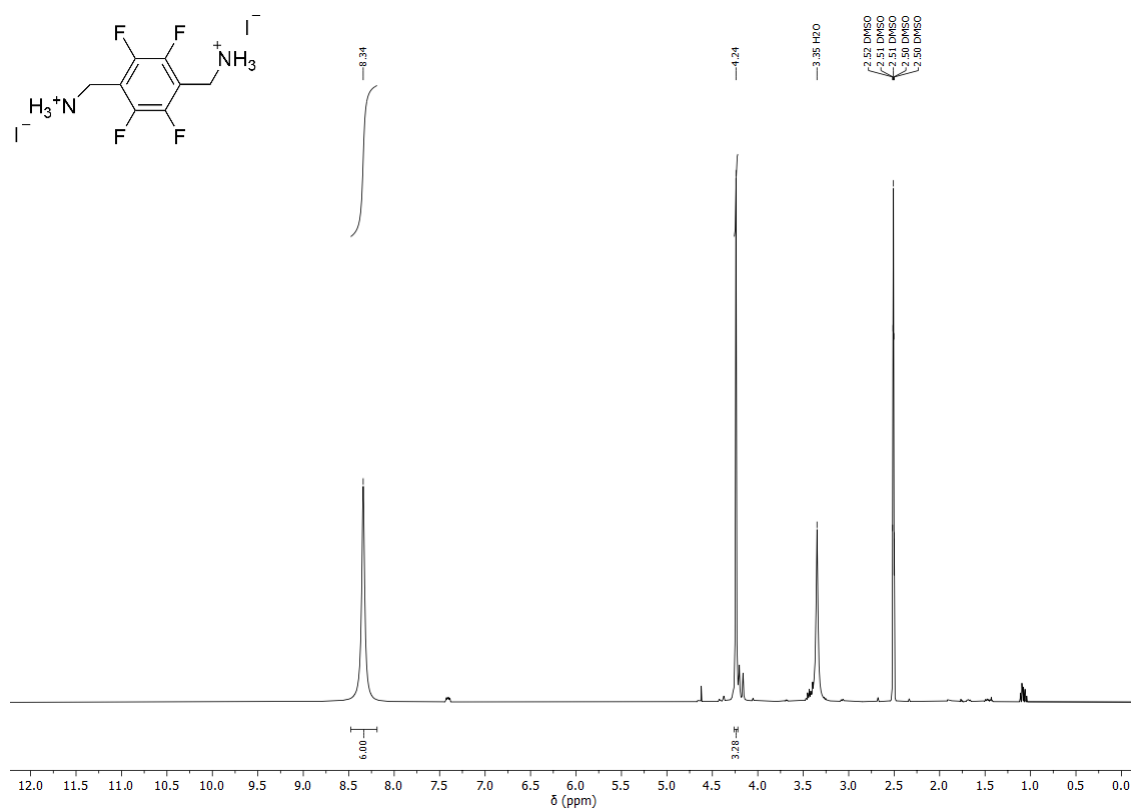


Figure S4. ^1H NMR of F-PDMAI in $(\text{CD}_3)_2\text{SO}$ (400 MHz, 298 K).

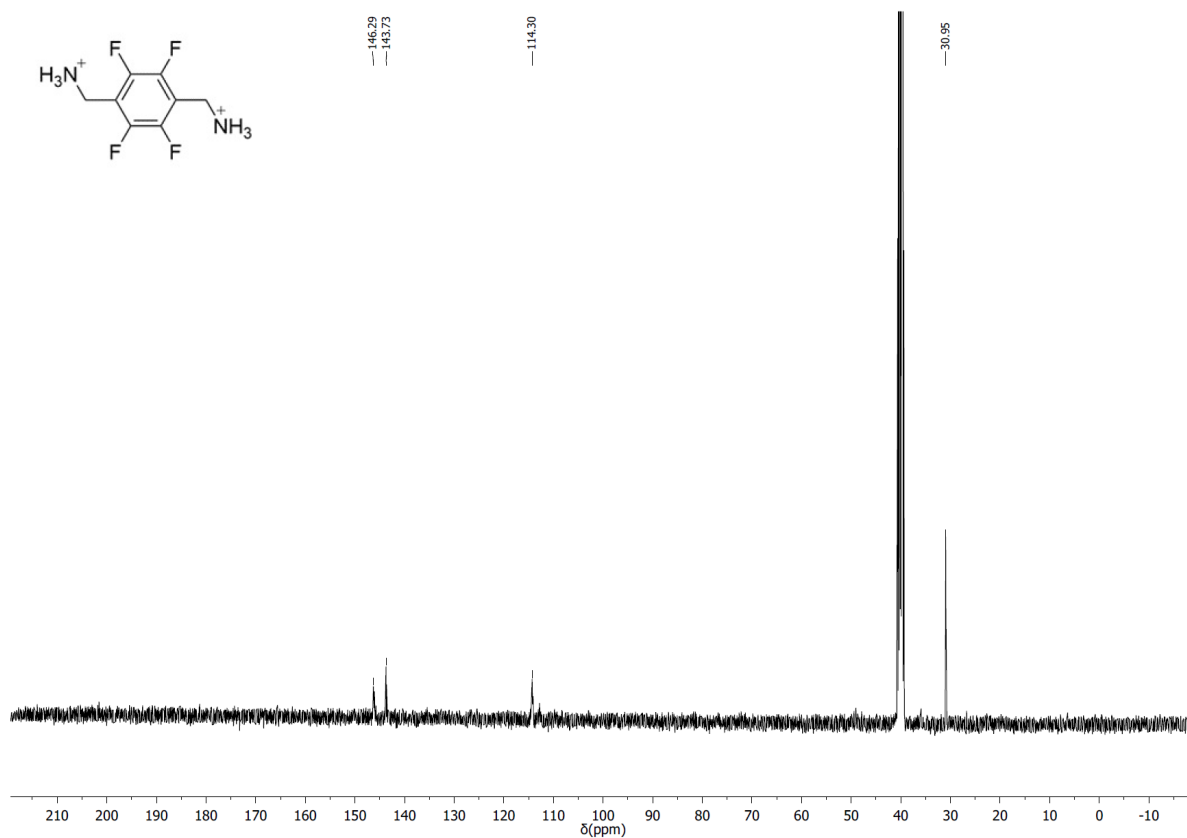


Figure S5. ¹³C NMR of F-PDMAI₂ in (CD₃)₂SO (101 MHz, 298 K).

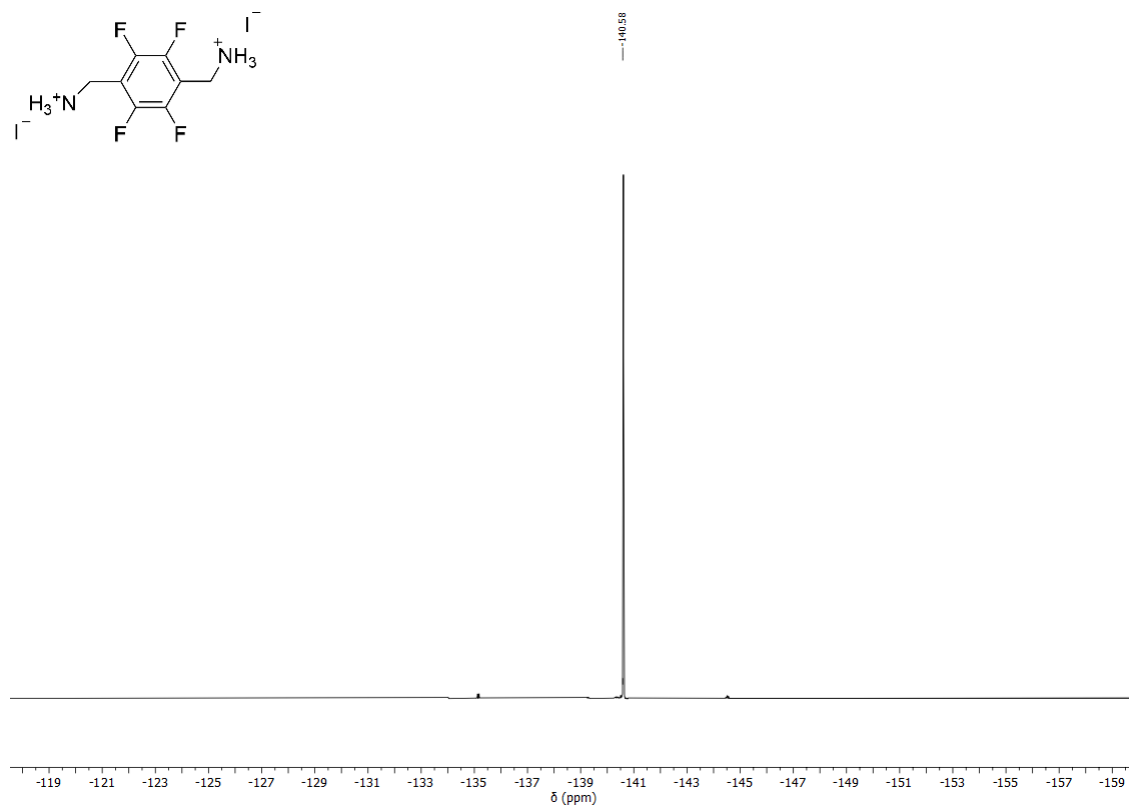


Figure S6. ¹⁹F NMR of F-PDMAI₂ in (CD₃)₂SO (377 MHz, 298 K).

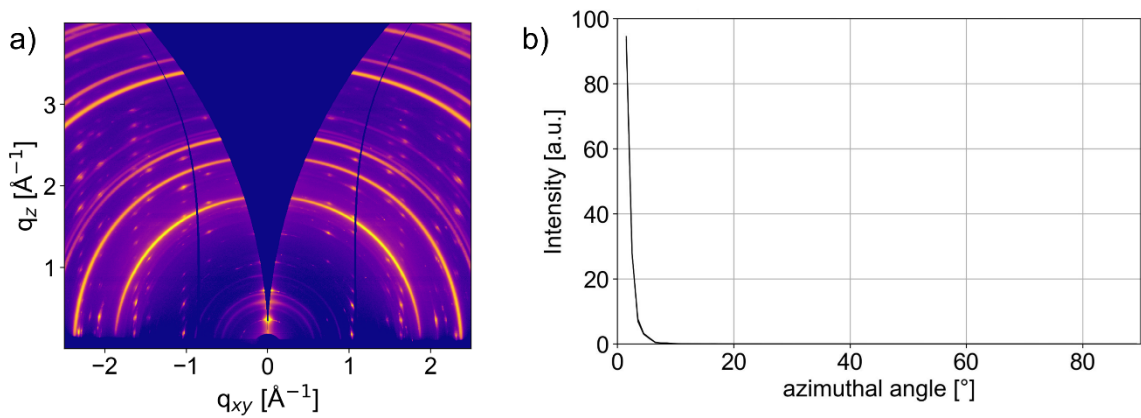


Figure S7. (a) GIWAXS reciprocal space maps of (F-BNA)₂PbI₄ film on glass and (b) the azimuthal profile of its first XRD peak at 0.35 \AA^{-1} .

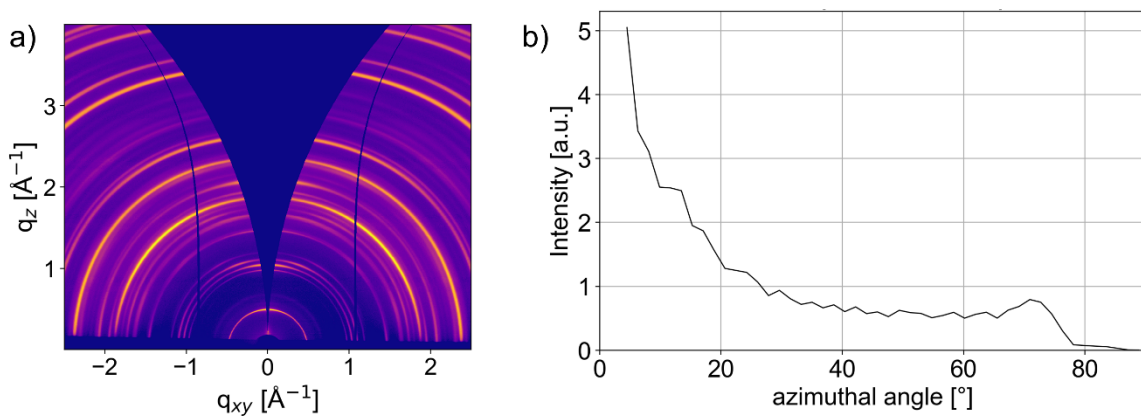


Figure S8. (a) GIWAXS reciprocal space maps of (F-PDMA)PbI₄ film on glass and (b) the azimuthal profile of its first XRD peak at 0.49 \AA^{-1} .

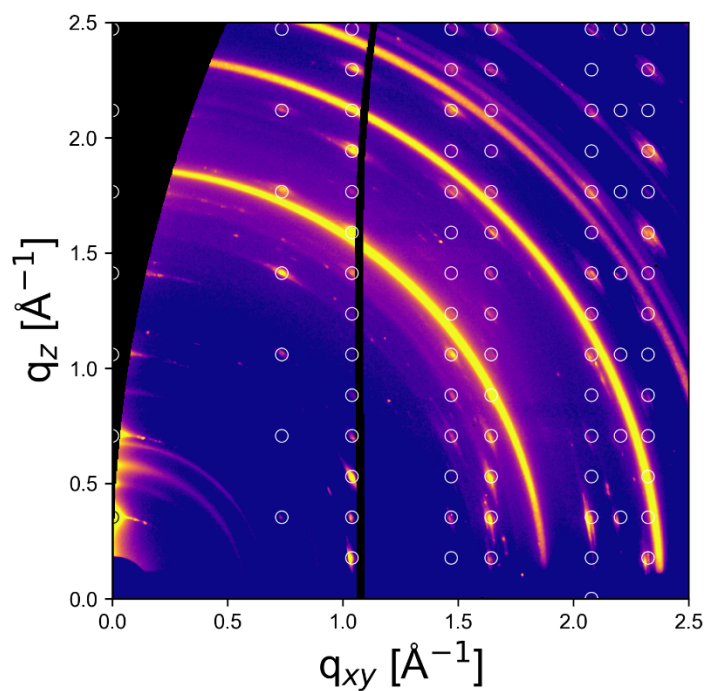


Figure S9. GIWAXS reciprocal space maps of (F-BNA)₂PbI₄ film on FTO covered glass. Circles correspond to the unit in Table S1 and coincide well with peaks from the 2D structure. Intense rings in the data originate from the FTO substrate.

Table S1. Unit cell parameters for (FBNA)₂PbI₄ (Error bars are estimated). Due to the fluorination of the spacer molecule, the unit cell is significantly larger than the unit cell of (BNA)₂PbI₄.⁴

Crystal Data	(FBNA) ₂ PbI ₄	(BNA) ₂ PbI ₄
a (Å)	8.55(8)	9.1561(5)
b (Å)	8.55(8)	8.6894(3)
c (Å)	35.6(4)	28.7762(15)
α (°)	90.0(5)	90
β (°)	90.0(5)	90.000(4)
γ (°)	90.0(5)	90
V (Å ³)	2602(78)	2289.46(19)

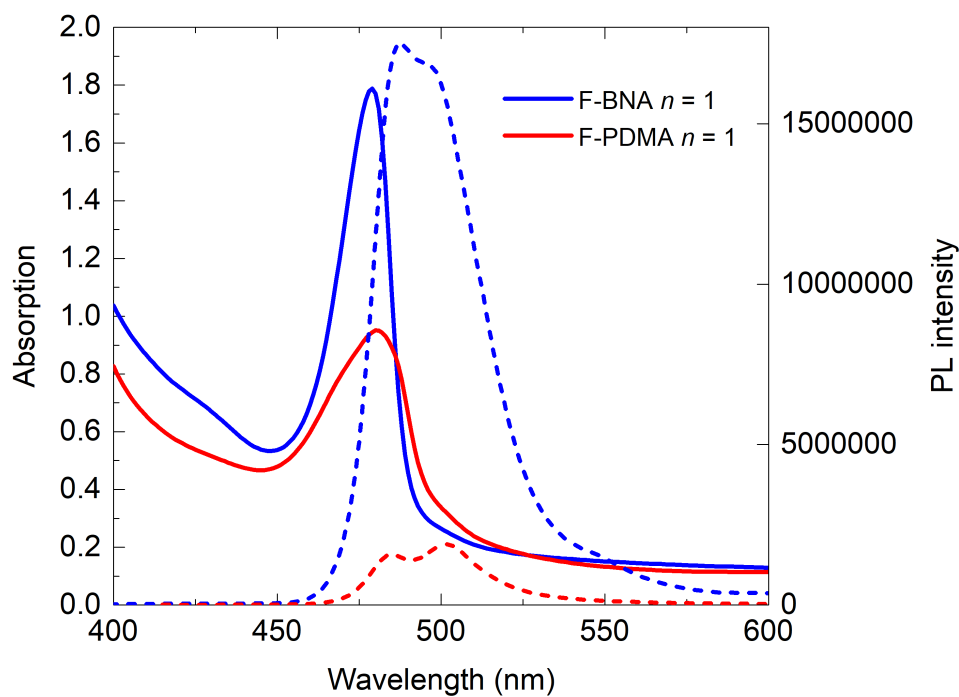


Figure S10. UV-vis absorption and PL raw spectra of the perfluoroarene-based 2D perovskite films of $n = 1$ nominal composition.

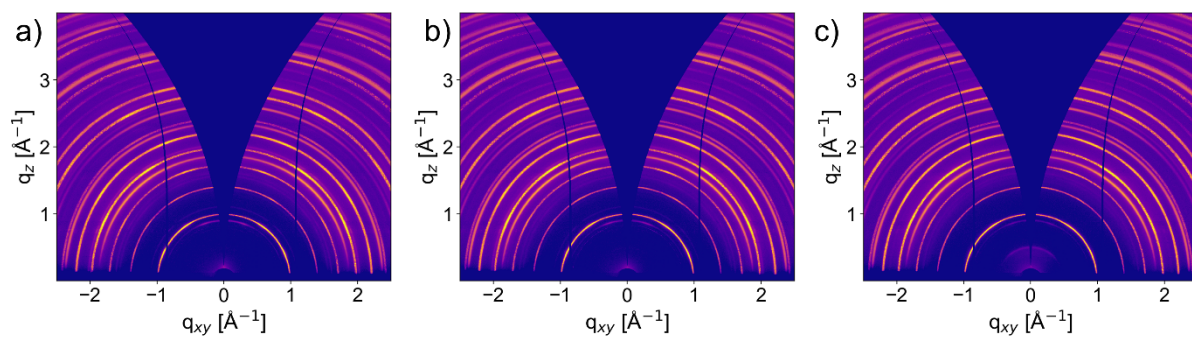


Figure S11. GIWAXS reciprocal space maps of (a) Control 3D, (b) (F-BNA)- and (c) (F-PDMA)- treated films on glass.

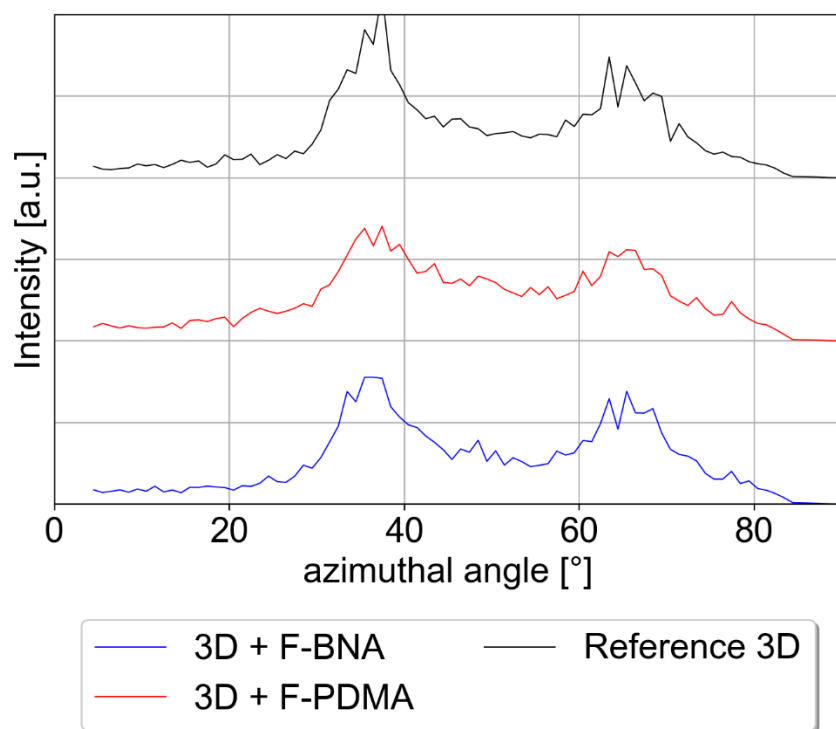


Figure S12 Azimuthal intensity profiles of the (001) perovskite peak from Figure S11.

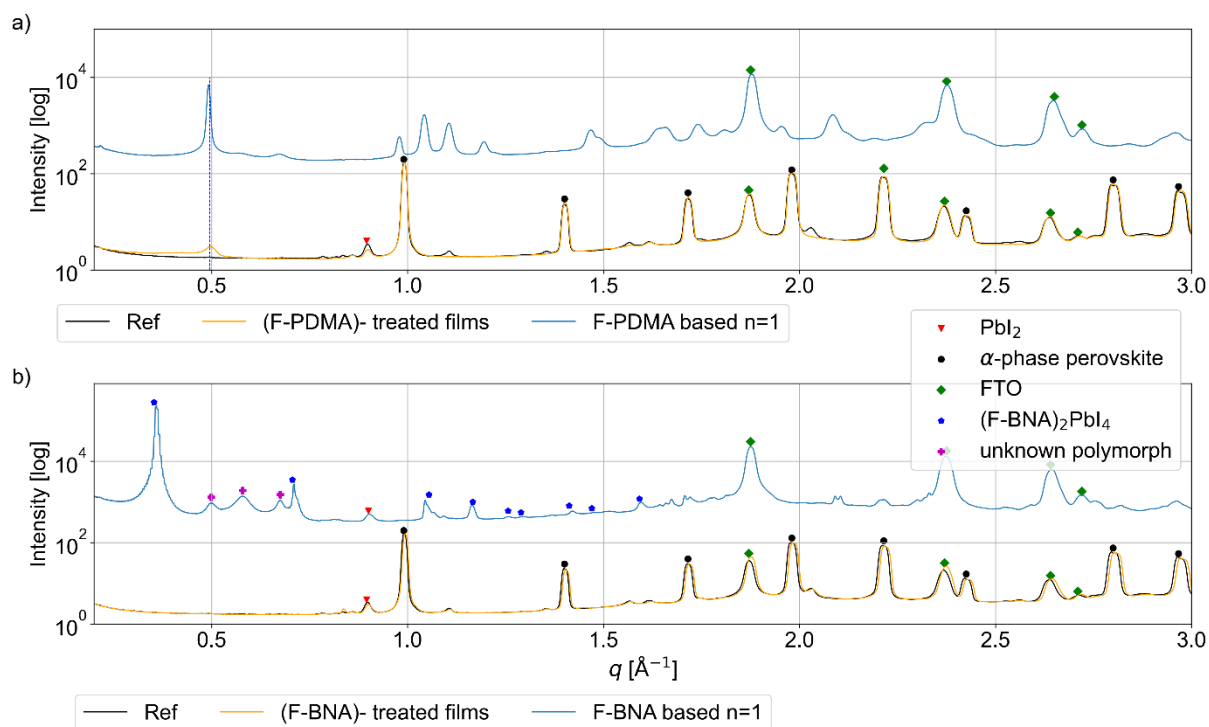


Figure S13. Radially integrated GIWAXS data of the a) (F-PDMA)PbI₄, Control and (F-PDMA)- treated film and b) (F-BNA)PbI₄, Control and (F-BNA)- treated film. Peaks marked with purple squares presumably originate from an (F-BNA)PbI₄ polymorph with low volume fraction.

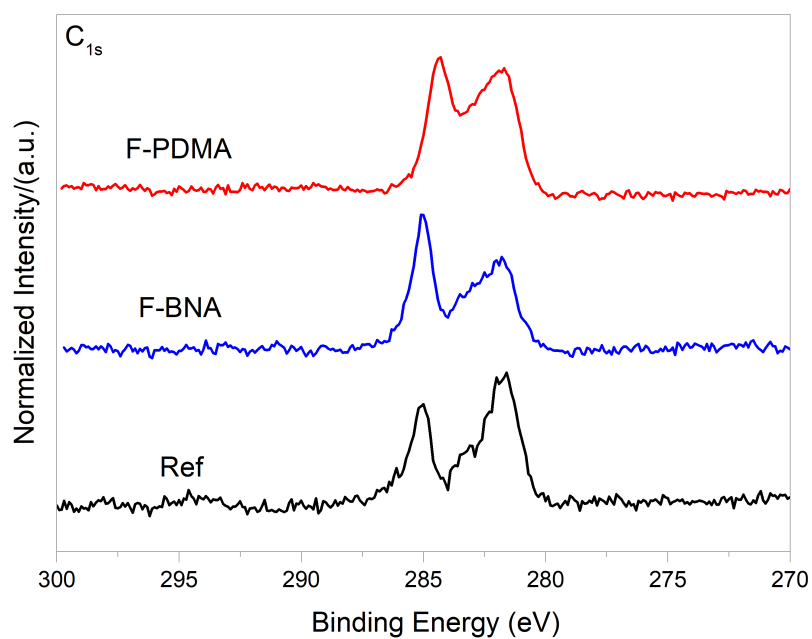


Figure S14. XPS C 1s core level spectra of the 3D perovskite films (Ref) and 3D/2D films with either F-PDMAI₂ (red) or F-BNAI (blue) overlayer on FTO glass.

Table S2. Full width at half maximum (FWHM) for XPS N 1s core level spectra (Figure 2d).

	FWHM (°)
F-PDMA	1.18
F-BNA	1.04
Reference	0.988

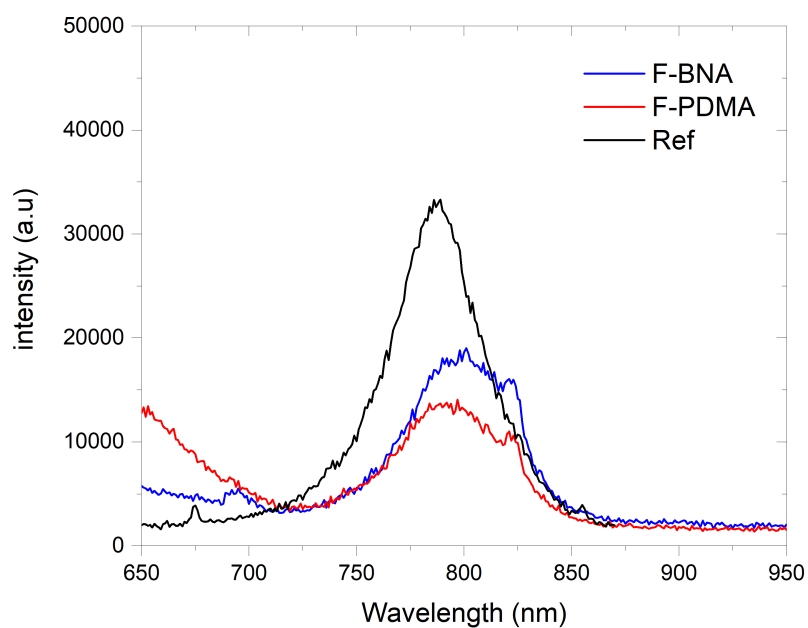


Figure S15. PL spectra of the 3D perovskite films (Ref) and 3D/2D films with either F-PDMAI₂ (red) or F-BNAI (blue) overlayer on microscope glass.

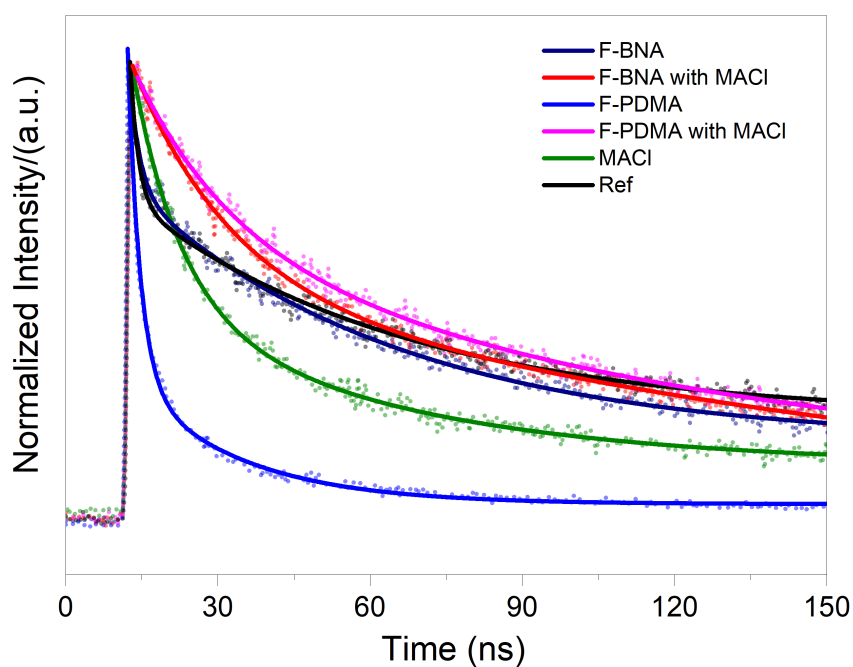


Figure S16. TRPL spectra of the 3D perovskite films (reference) and the 3D perovskite films treated with MACI additive and 3D/2D films with F-PDMAI₂ or F-BNAI overlayers on glass.

Table S3. Summary of the parameters from fitting to the TRPL decay data (without HTM)

	$\tau_1(\text{ns})$	$\tau_2(\text{ns})$
Ref	1.6	53.8
F-BNA	2	52.96
F-PDMA	21.81	2.44
Ref With MACl	9.49	51.14
F-BNA With MACl	0.58	19.65
F-PDMA With MACl	144.84	19.03

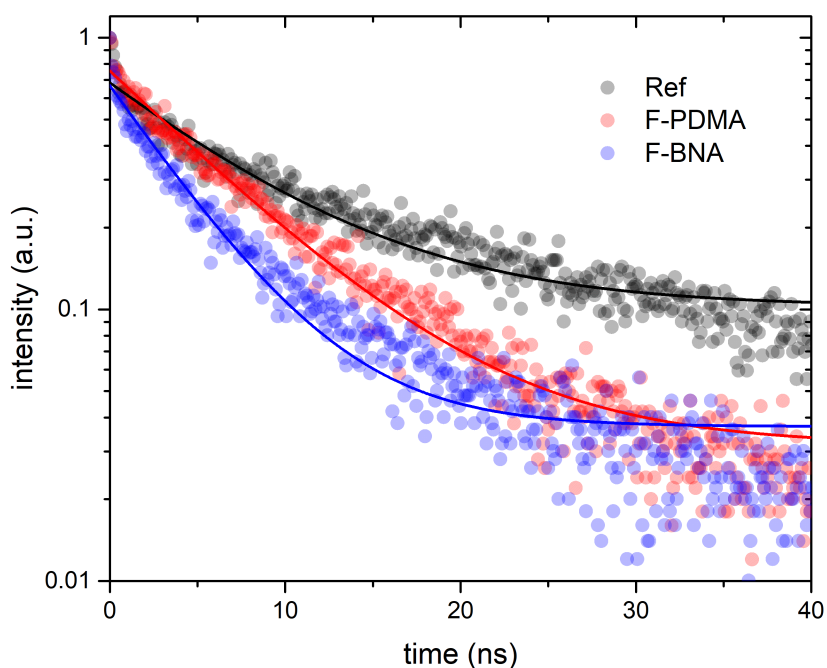


Figure S17. TRPL spectra of the 3D perovskite films (Ref) and 3D/2D films with either F-PDMAI₂ (red) or F-BNAI (blue) overlayer on microscope glass with HTM on top.

Table S4. Summary of the parameters from the fit of the TRPL decay (with HTM).

	$\tau_1(\text{ns})$
Ref	7.9
F-BNA	4.6
F-PDMA	6.8

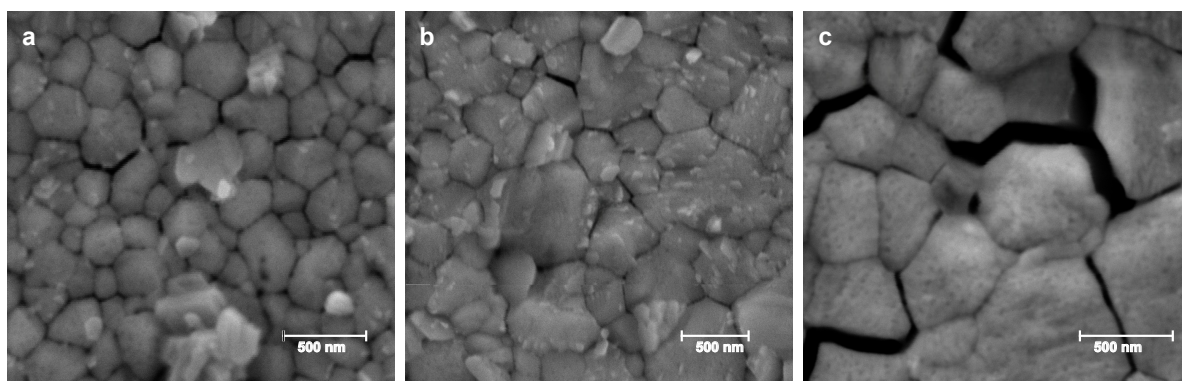


Figure S18. SEM image of the perovskite surface based on (a) 3D films (Ref) and (b–c) 2D/3D films treated with either F-BNAI (b) and (c) F-PDMAI₂ no FTO glass.

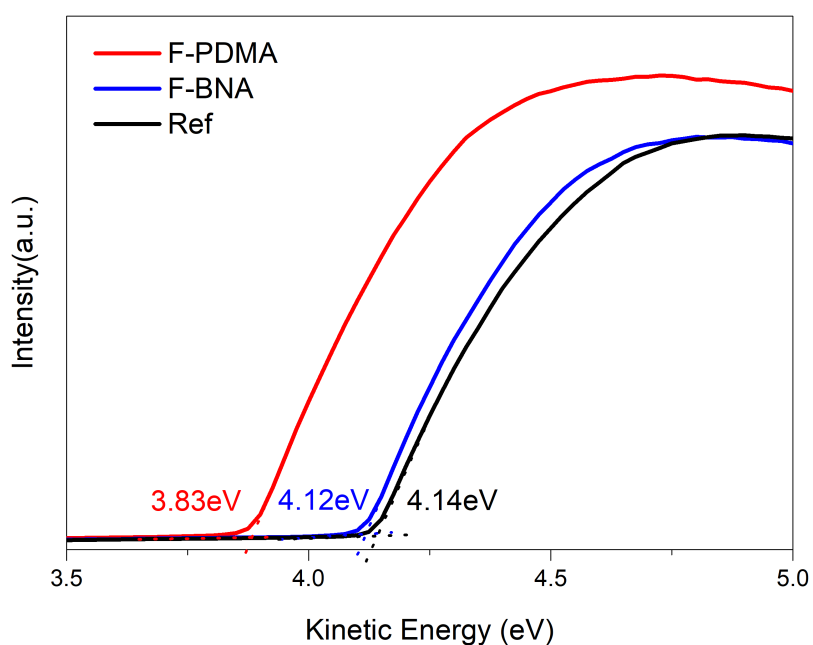


Figure S19. UPS spectra determining the kinetic energy around the secondary electron cut-off of the control (Ref) and treated (F-BNA or F-PDMA) perovskite films on FTO glass.

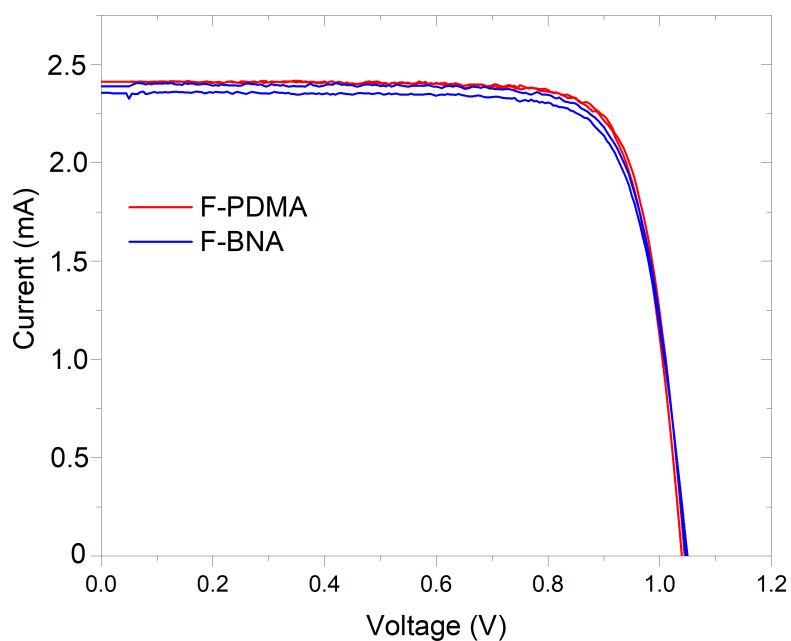


Figure S20. Current-voltage characteristics of the champion perovskite solar cells based on $(\text{Cs}_{0.05}\text{FA}_{0.85}\text{MA}_{0.10})\text{Pb}(\text{I}_{0.97}\text{Br}_{0.03})_3$ with an overlayer of F-BNAI or F-PDMAI₂.

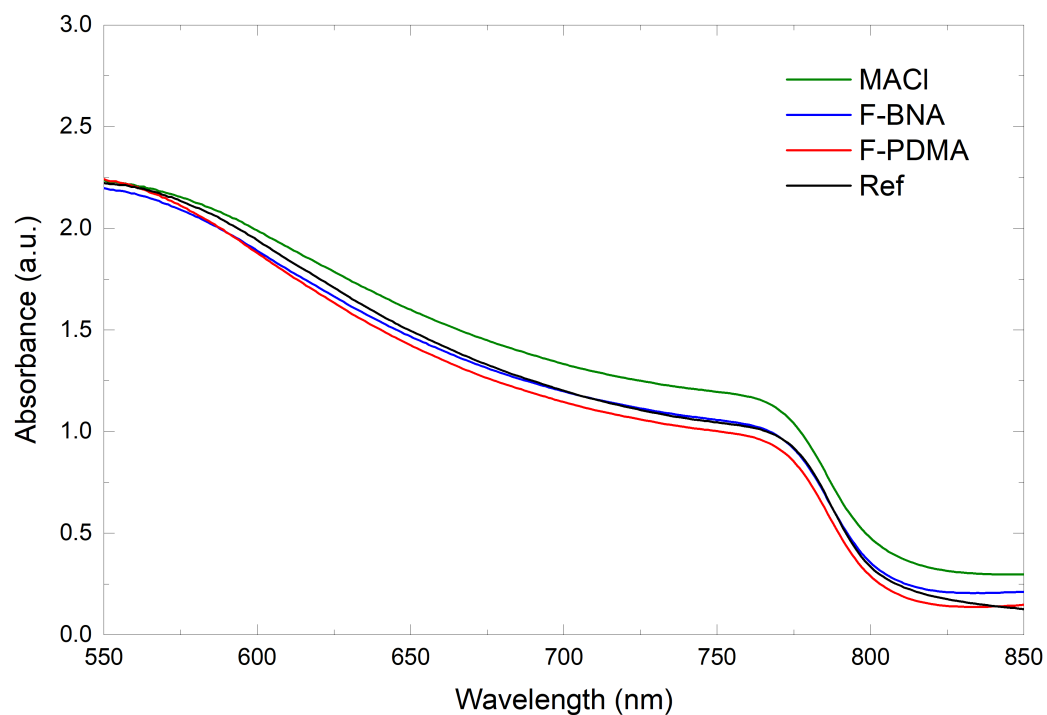


Figure S21. UV-vis spectra of the 3D perovskite films (Ref) and 3D/2D films with either F-PDMAI₂ (red) or F-BNAI (blue) overlayer in the presence of MACI additive on glass.

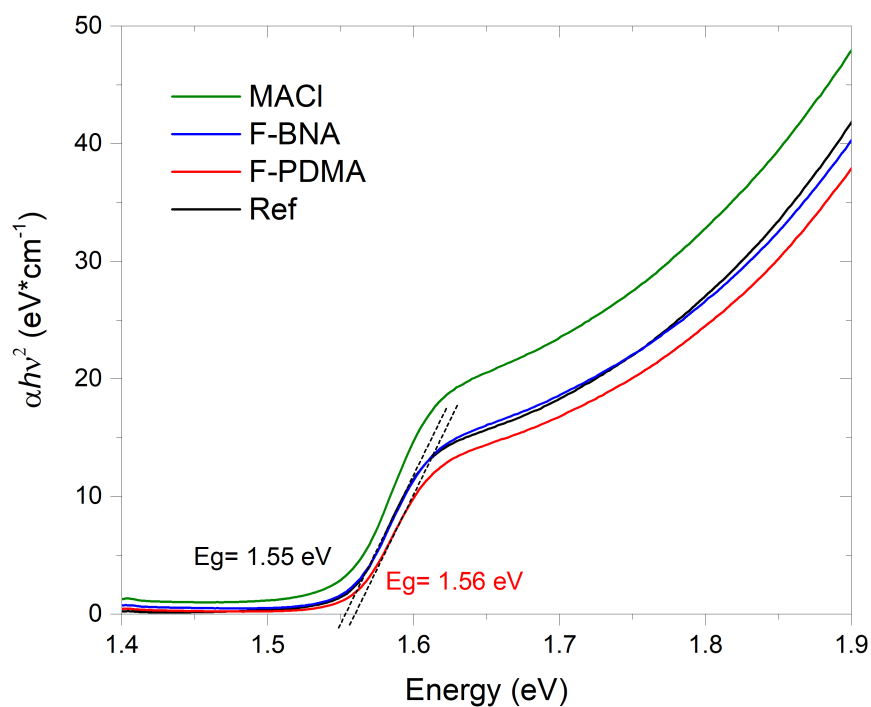


Figure S22. Tauc plot determining the optical band gap (E_g) for the 3D perovskite films (Ref) and 3D/2D films with either F-PDMAI₂ (red) or F-BNAI (blue) overlayer in the presence of MACI additive on glass.

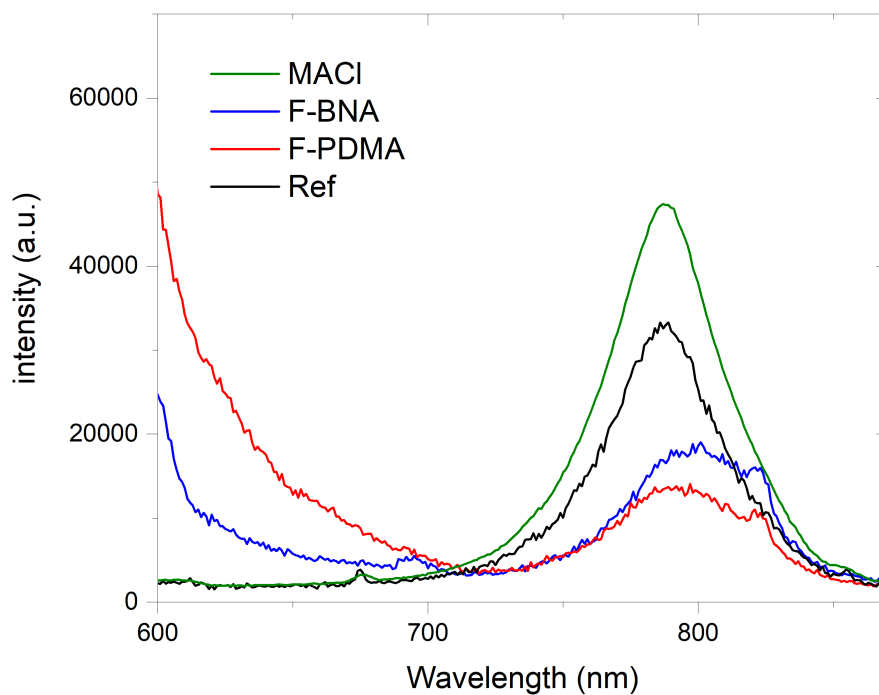


Figure S23. PL spectra of the 3D perovskite films (Ref) and 3D/2D films with either F-PDMAI₂ (red) or F-BNAI (blue) overlayer in the presence of MACI additive on microscope glass.

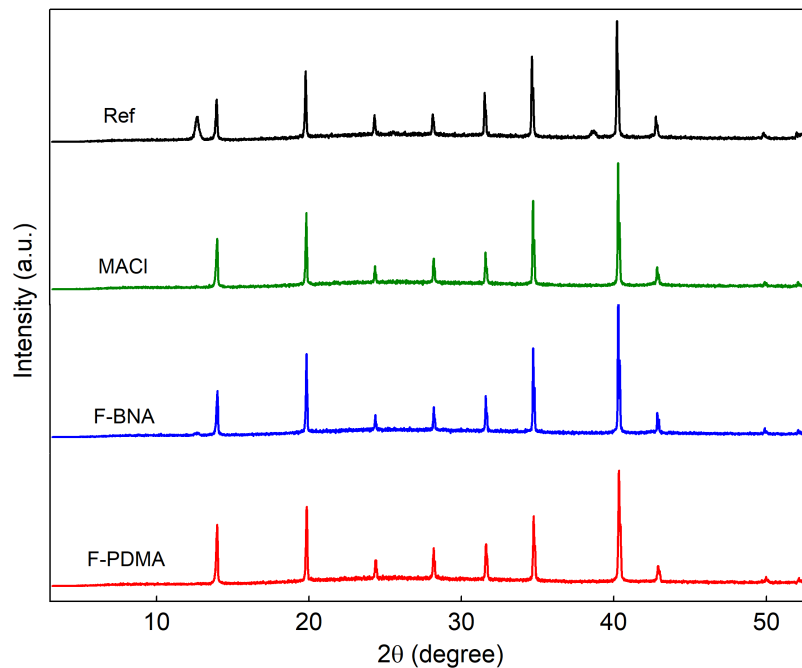


Figure S24. XRD pattern of the 3D perovskite films (Ref) and 3D/2D films with either F-PDMAI₂ (red) or F-BNAI (blue) overlayer in presence of MACl additive on microscope glass.

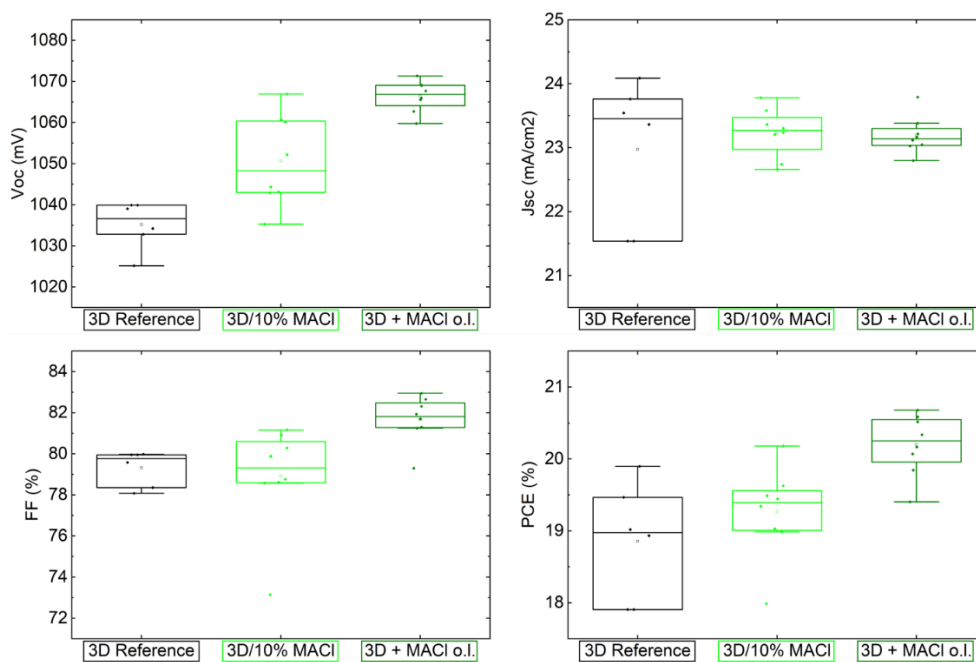


Figure. S25. Statistical distribution of photovoltaic metric, including open-circuit voltage (V_{oc}), short-circuit current density (J_{sc}), fill factor (FF), and power conversion efficiency (PCE) for control (3D Reference) and MACl-treated devices as an additive (10%) and an overlayer (o.l.).

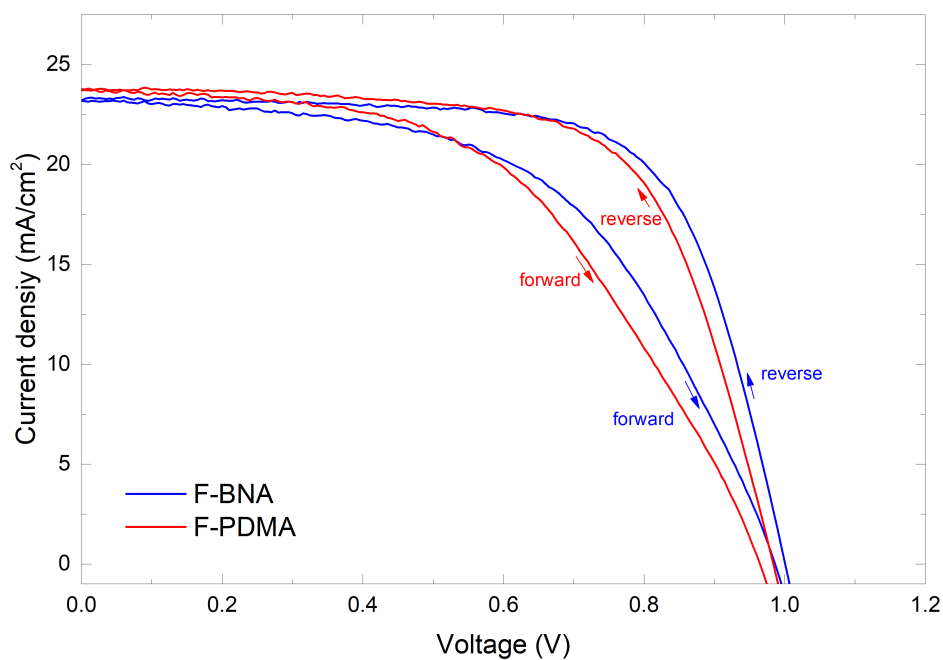


Figure S26. Current-voltage characteristics of the champion perovskite solar cells based on $\text{Cs}_{0.05}\text{FA}_{0.85}\text{MA}_{0.10}\text{Pb}(\text{I}_{0.97}\text{Br}_{0.03})_3$ with MACl additive treated with F-BNAI or F-PDMAI₂.

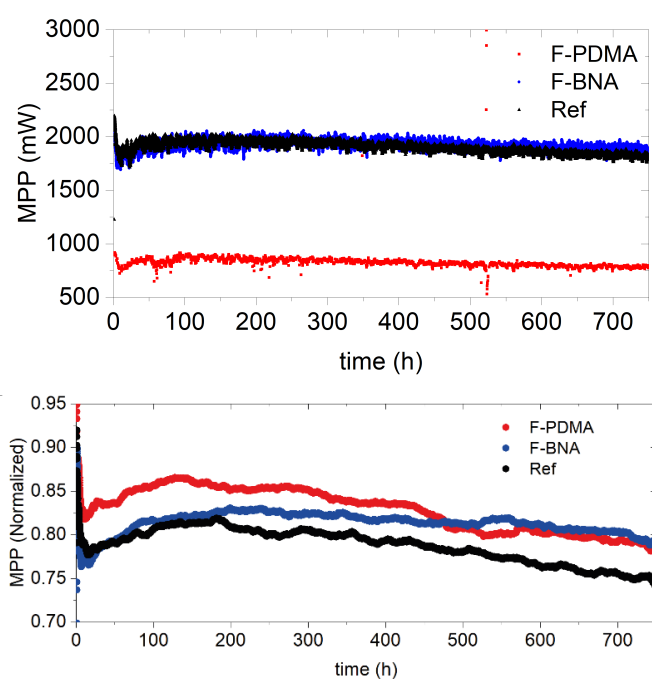


Figure S27. Evolution of the PCE during operation by MPP tracking (top) and normalized performance (bottom) of control (black), F-BNA (blue) and F-PDMA (red) treated perovskite solar cells in N_2 atmosphere under 1 sun irradiation at ambient temperature.

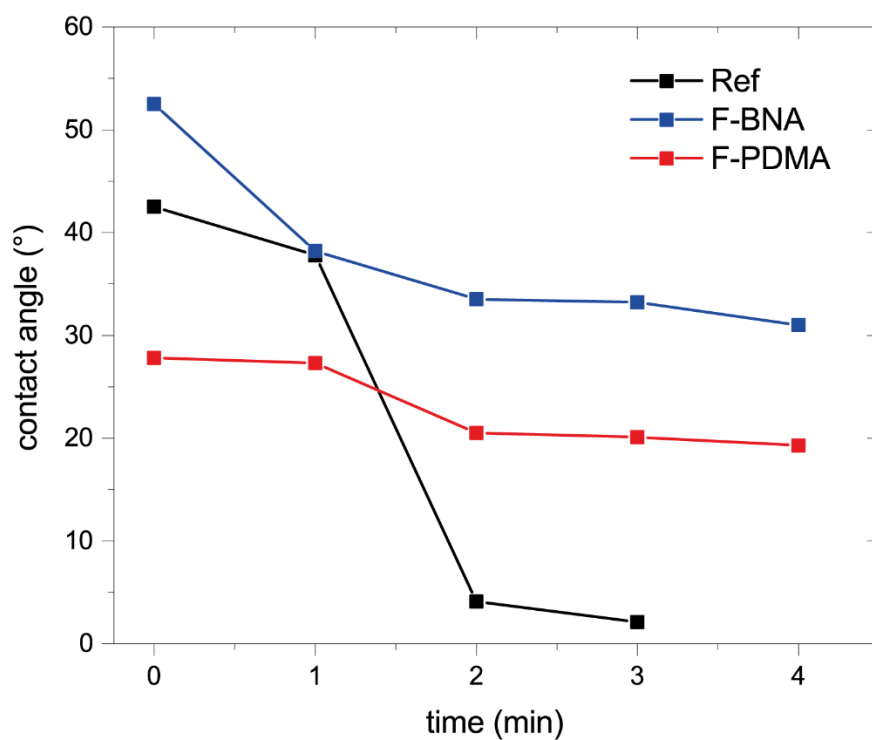
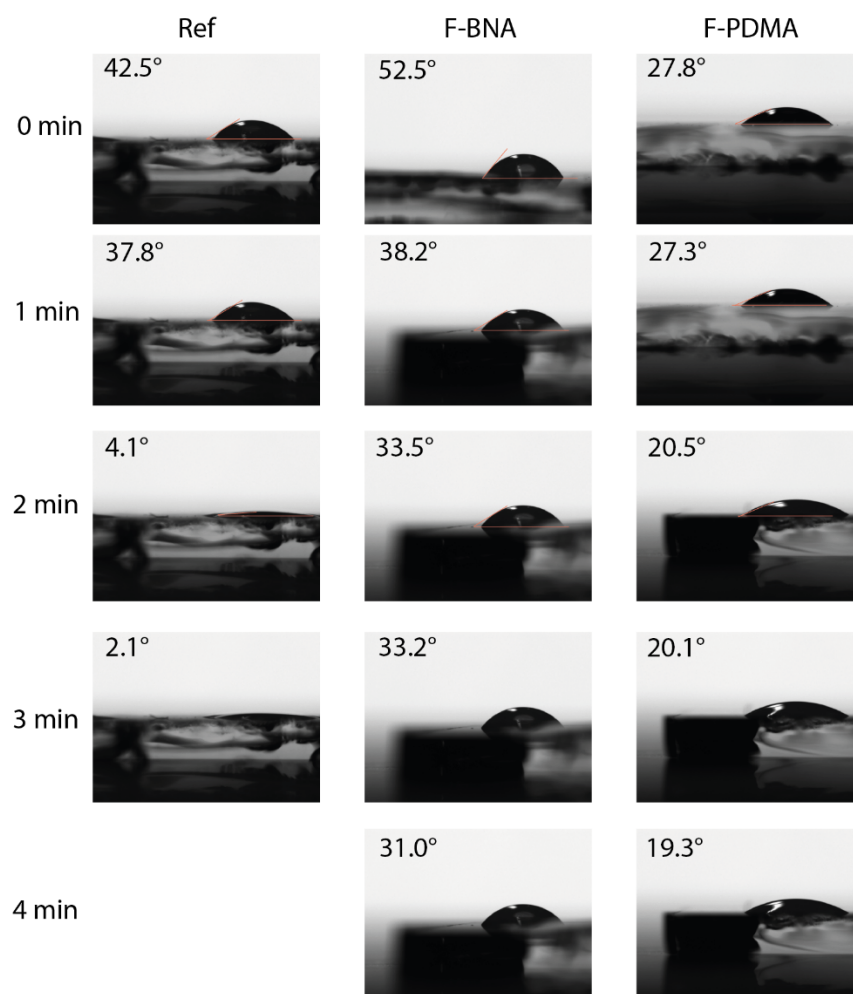


Figure S28. Contact angle measurement of a water drop on the surface of 3D perovskite films (Ref) and 3D/2D films with either F-PDMAI₂ (red) or F-BNAI (blue) overlayer on glass.

Table S5. Summary of the photovoltaic parameters of the champion devices.

Device	V _{oc} (V)	J _{sc} (μA)	FF	PCE
Control	1.05	2183	80.0%	18.4%
F-BNA	1.06	2389	80.1%	20.0%
F-PDMA	1.05	2413	79.9%	20.0%

Reference

- (1) Almalki, M.; Dučinskas, A.; Carbone, L. C.; Pfeifer, L.; Piveteau, L.; Luo, W.; Lim, E.; Gaina, P. A.; Schouwink, P. A.; Zakeeruddin, S. M. Nanosegregation in arene-perfluoroarene π -systems for hybrid layered Dion–Jacobson perovskites. *Nanoscale* **2022**, *14*, 6771–6776.
- (2) Hope, M. A.; Nakamura, T.; Ahlawat, P.; Mishra, A.; Cordova, M.; Jahanbakhshi, F.; Mladenović, M.; Runjhun, R.; Merten, L.; Hinderhofer, A.; Carlsen, B. I.; Kubicki, D. J.; Gershoni-Poranne, R.; Schneeberger, T.; Carbone, L. C.; Liu, Y.; Zakeeruddin, S. M.; Lewinski, J.; Hagfeldt, A.; Schreiber, F.; Rothlisberger, U.; Grätzel, M.; Milić, J. V.; Emsley, L. Nanoscale Phase Segregation in Supramolecular π -Templating for Hybrid Perovskite Photovoltaics from NMR Crystallography. *J. Am. Chem. Soc.* **2021**, *143*, 1529–1538.
- (3) Li, Y.; Milić, J. V.; Ummadisingu, A.; Seo, J.-Y.; Im, J.-H.; Kim, H.-S.; Liu, Y.; Dar, M. I.; Zakeeruddin, S. M.; Wang, P.; Hagfeldt, A.; Grätzel, M. Bifunctional Organic Spacers for Formamidinium-Based Hybrid Dion–Jacobson Two-Dimensional Perovskite Solar Cells. *Nano Lett.* **2019**, *19*, 150–157.
- (4) Mao, L.; Tsai, H.; Nie, W.; Ma, L.; Im, J.; Stoumpos, C. C.; Malliakas, C. D.; Hao, F.; Wasielewski, M. R.; Mohite, A. D.; Kanatzidis, M. G. Role of Organic Counterion in Lead- and Tin-Based Two-Dimensional Semiconducting Iodide Perovskites and Application in Planar Solar Cells. *Chem. Mater.* **2016**, *28*, 7781–7792.